



| | |
|-------------------------------|---|
| Publication Year | 2017 |
| Acceptance in OA @INAF | 2021-02-02T14:11:42Z |
| Title | The Hubble Space Telescope UV Legacy Survey of Galactic globular clusters - IX. The Atlas of multiple stellar populations |
| Authors | Milone, A. P.; Piotto, G.; Renzini, A.; Marino, A. F.; BEDIN, Luigi; et al. |
| DOI | 10.1093/mnras/stw2531 |
| Handle | http://hdl.handle.net/20.500.12386/30160 |
| Journal | MONTHLY NOTICES OF THE ROYAL ASTRONOMICAL SOCIETY |
| Number | 464 |

The *Hubble Space Telescope* UV Legacy Survey of Galactic globular clusters – IX. The Atlas of multiple stellar populations

A. P. Milone,^{1★} G. Piotto,^{2,3} A. Renzini,³ A. F. Marino,¹ L. R. Bedin,³ E. Vesperini,⁴
F. D’Antona,⁵ D. Nardiello,² J. Anderson,⁶ I. R. King,⁷ D. Yong,¹ A. Bellini,⁶
A. Aparicio,^{8,9} B. Barbuy,¹⁰ T. M. Brown,⁶ S. Cassisi,¹¹ S. Ortolani,²
M. Salaris,¹² A. Sarajedini¹³ and R. P. van der Marel⁶

¹Research School of Astronomy and Astrophysics, Australian National University, Mt Stromlo Observatory, via Cotter Rd, Weston, ACT 2611, Australia

²Dipartimento di Fisica e Astronomia ‘Galileo Galilei’, Univ. di Padova, Vicolo dell’Osservatorio 3, Padova I-35122, Italy

³Istituto Nazionale di Astrofisica – Osservatorio Astronomico di Padova, Vicolo dell’Osservatorio 5, Padova I-35122, Italy

⁴Department of Astronomy, Indiana University, Bloomington, IN 47405, USA

⁵Istituto Nazionale di Astrofisica – Osservatorio Astronomico di Roma, Via Frascati 33, I-00040 Monteporzio Catone, Roma, Italy

⁶Space Telescope Science Institute, 3800 San Martin Drive, Baltimore, MD 21218, USA

⁷Department of Astronomy, University of Washington, Box 351580, Seattle, WA 98195-1580, USA

⁸Instituto de Astrofísica de Canarias, E-38200 La Laguna, Tenerife, Canary Islands, Spain

⁹Department of Astrophysics, University of La Laguna, E-38200 La Laguna, Tenerife, Canary Islands, Spain

¹⁰IAG, Universidade de Sao Paulo, Rua de Matao 1226, Cidade Universitaria, Sao Paulo 05508-900, Brazil

¹¹Istituto Nazionale di Astrofisica – Osservatorio Astronomico di Teramo, Via Mentore Maggini s.n.c., I-64100 Teramo, Italy

¹²Astrophysics Research Institute, Liverpool John Moores University, Liverpool Science Park, IC2 Building, 146 Brownlow Hill, Liverpool L3 5RF, UK

¹³Department of Astronomy, University of Florida, 211 Bryant Space Science Center, Gainesville, FL 32611, USA

Accepted 2016 October 3. Received 2016 September 29; in original form 2016 July 22; Editorial Decision 2016 September 29

ABSTRACT

We use high-precision photometry of red-giant-branch (RGB) stars in 57 Galactic globular clusters (GCs), mostly from the ‘*Hubble Space Telescope* (HST) UV Legacy Survey of Galactic GCs’, to identify and characterize their multiple stellar populations. For each cluster the pseudo-two-colour diagram (or ‘chromosome map’) is presented, built with a suitable combination of stellar magnitudes in the *F*275W, *F*336W, *F*438W, and *F*814W filters that maximizes the separation between multiple populations. In the chromosome map of most GCs (type-I clusters), stars separate in two distinct groups that we identify with the first (1G) and the second generation (2G). This identification is further supported by noticing that 1G stars have primordial (oxygen-rich, sodium-poor) chemical composition, whereas 2G stars are enhanced in sodium and depleted in oxygen. This 1G–2G separation is not possible for a few GCs where the two sequences have apparently merged into an extended, continuous sequence. In some GCs (type-II clusters) the 1G and/or the 2G sequences appear to be split, hence displaying more complex chromosome maps. These clusters exhibit multiple subgiant branches (SGBs) also in purely optical colour–magnitude diagrams, with the fainter SGB joining into a red RGB which is populated by stars with enhanced heavy-element abundance. We measure the RGB width by using appropriate colours and pseudo-colours. When the metallicity dependence is removed, the RGB width correlates with the cluster mass. The fraction of 1G stars ranges from ~8 per cent to ~67 per cent and anticorrelates with the cluster mass, indicating that incidence and complexity of the multiple population phenomenon both increase with cluster mass.

Key words: techniques: photometric – stars: abundance – stars: Population II – globular clusters: general.

* E-mail: antonino.milone@anu.edu.au

1 INTRODUCTION

The formation of globular clusters (GCs) and the origin of their ubiquitous multiple stellar populations remain a major astrophysical challenge. In this series of papers, we build on the *Hubble Space Telescope* (*HST*) UV Legacy Survey of Galactic GCs (Piotto et al. 2015, hereafter *Paper I* of this series) to fully document the complexity of the multiple populations. This phenomenon is most effectively characterized when combining ultraviolet and optical *HST* photometry, as documented by pilot studies by our group (e.g. Milone et al. 2012b, 2013; Piotto et al. 2013). These studies have demonstrated that appropriate combinations of ultraviolet and optical filters, to construct e.g. $m_{F275W} - m_{F336W}$ versus $m_{F336W} - m_{F438W}$ two-colour diagrams or the m_{F814W} plot versus the pseudo-colour $C_{F275W, F336W, F438W} = (m_{F275W} - m_{F336W}) - (m_{F336W} - m_{F438W})$, very efficiently identify multiple stellar populations in GCs (see *Paper I* for a general introduction into the subject).

In other papers (Milone et al. 2015a, Milone et al. 2015b, hereafter *Papers II* and *III*), we have shown that the combination of the $C_{F275W, F336W, F438W}$ pseudo-colour with the $m_{F275W} - m_{F814W}$ colour maximizes the separation between stellar populations along the main sequence (MS) and the red giant branch (RGB) and have used this diagram to identify and characterize seven distinct stellar populations in NGC 7089 (*Paper II*) and at least five populations in NGC 2808 (*Paper III*). In *Paper IV* of this series we provided accurate determination of the GC helium abundance and ages of stellar populations in NGC 6352 (Nardiello et al. 2015a), while in *Paper V* we have exploited the first results from our survey to set constraints on the formation scenarios (Renzini et al. 2015). Other papers of this series include the study of the internal dynamics of multiple populations (Bellini et al. 2015, *Paper VI*) and of the horizontal branch (HB) morphology (Brown et al. 2016, *Paper VII*). An early-stage data release of the photometric and astrometric data is provided in *Paper VIII* by Soto et al. (submitted).

In this paper, we identify and characterize multiple stellar populations along the RGB for the entire sample of 57 GCs. The paper is organized as follows. Data reduction and analysis are briefly described in Section 2. In Section 3, we measure the intrinsic RGB width in $C_{F275W, F336W, F438W}$ and $m_{F275W} - m_{F814W}$ for all the clusters and we describe how to combine these two quantities to construct ‘chromosome maps’, which most efficiently identify the distinct stellar populations hosted by each individual GC. The chromosome maps of all the clusters are presented in Section 4. We distinguish between putative first and second generations of stars (respectively 1G and 2G) and measure the fraction of 1G stars over the total cluster population. A group of GCs exhibiting particularly complex chromosome maps and characterized by the presence of a multimodal subgiant branch (SGB) are further investigated in Section 5. In Section 6, we present univariate relations between the global parameters of the host clusters, the RGB width and the population ratio. Summary and conclusions follow in Section 7.

2 DATA AND DATA ANALYSIS

This study is mostly based on data from the *HST* program GO-13297 (PI. G. Piotto) and data from the pilot programs GO-12605 and GO-11233 from the same PI. The aim of these programs is to derive high-precision photometry and astrometry of stars in 57 clusters through the $F275W$, $F336W$, and $F438W$ filters of the *HST* Ultraviolet and Visual Channel of the Wide Field Camera 3 (WFC3/UVIS). In addition to data and catalogues illustrated in *Paper I*, we make use of $F606W$ and $F814W$ photometry from the Wide Field Channel of the Advanced Camera for Survey (WFC/ACS) which is available for all clusters, mainly from the ACS survey of Galactic GCs (GO-10775, PI. A. Sarajedini, see Sarajedini et al. 2007). In order to improve the quality of the photometry for a few clusters, we have included additional archival WFC3/UVIS images in $F275W$, $F336W$, and $F438W$ as reported in Table 1.

Table 1. Description of the archive *HST* images set that has been used in this paper in addition to GO-10775, GO-11233, GO-12605, and GO-13297 data.

| Cluster | Date | $N \times$ Exp time | Filter | Instrument | Program | PI |
|----------|------------------------------------|--|---------|------------|---------|---------------|
| NGC 0104 | 2002 September 30–November 10 | $3 \times 150 \text{ s} + 6 \times 100 \text{ s} + 10 \text{ s}$ | $F435W$ | WFC/ACS | 9281 | J. Grindlay |
| NGC 0104 | 2002 September 30–July 07 | 100 s | $F435W$ | WFC/ACS | 9443 | I. King |
| NGC 0104 | 2010 September 28–29 | $2 \times 580 \text{ s} + 30 \text{ s}$ | $F336W$ | WFC3/UVIS | 11729 | W. Freedman |
| NGC 0104 | 2012 November 14–2013 September 20 | $9 \times 485 \text{ s} + 9 \times 720 \text{ s}$ | $F336W$ | WFC3/UVIS | 12971 | H. Richer |
| NGC 5139 | 2009 July 15 | $9 \times 350 \text{ s} + 35 \text{ s}$ | $F275W$ | WFC3/UVIS | 11452 | J. K. Quijano |
| NGC 5139 | 2010 January 12–July 04 | $22 \times 800 \text{ s}$ | $F275W$ | WFC3/UVIS | 11911 | E. Sabbi |
| NGC 5139 | 2011 February 14–March 24 | $8 \times 800 \text{ s}$ | $F275W$ | WFC3/UVIS | 12339 | E. Sabbi |
| NGC 5139 | 2009 July 15 | $9 \times 350 \text{ s} + 35 \text{ s}$ | $F336W$ | WFC3/UVIS | 11452 | J. K. Quijano |
| NGC 5139 | 2010 January 10–July 04 | $19 \times 350 \text{ s}$ | $F336W$ | WFC3/UVIS | 11911 | E. Sabbi |
| NGC 5139 | 2011 February 14–15 | $9 \times 350 \text{ s}$ | $F336W$ | WFC3/UVIS | 12339 | E. Sabbi |
| NGC 5139 | 2012 July 26 | $8 \times 700 \text{ s} + 11 \times 10 \text{ s}$ | $F336W$ | WFC3/UVIS | 12802 | J. MacKenty |
| NGC 5139 | 2009 July 15 | 35 s | $F438W$ | WFC3/UVIS | 11452 | J. K. Quijano |
| NGC 5139 | 2010 January 14–July 04 | $25 \times 438 \text{ s}$ | $F438W$ | WFC3/UVIS | 11911 | E. Sabbi |
| NGC 5139 | 2011 February 15–March 24 | $9 \times 350 \text{ s}$ | $F438W$ | WFC3/UVIS | 12339 | E. Sabbi |
| NGC 5139 | 2009 July 15 | 35 s | $F814W$ | WFC3/UVIS | 11452 | J. K. Quijano |
| NGC 5139 | 2010 January 10–July 04 | $27 \times 40 \text{ s}$ | $F814W$ | WFC3/UVIS | 11911 | E. Sabbi |
| NGC 5139 | 2011 February 15–March 24 | $9 \times 40 \text{ s}$ | $F814W$ | WFC3/UVIS | 12339 | E. Sabbi |
| NGC 5927 | 2010 September 01 | $2 \times 475 \text{ s} + 30 \text{ s}$ | $F336W$ | WFC3/UVIS | 11729 | W. Freedman |
| NGC 6341 | 2010 October 11 | $2 \times 425 \text{ s} + 30 \text{ s}$ | $F336W$ | WFC3/UVIS | 11729 | W. Freedman |
| NGC 6352 | 2012 February 13 | $410 \text{ s} + 5 \times 400 \text{ s}$ | $F336W$ | WFC3/UVIS | 12746 | A. Kong |
| NGC 6362 | 2010 August 13 | $5 \times 450 \text{ s} + 368 \text{ s}$ | $F336W$ | WFC3/UVIS | 12008 | A. Kong |
| NGC 6397 | 2010 March 9–11 | $6 \times 620 \text{ s}$ | $F336W$ | WFC3/UVIS | 11633 | R. Rich |
| NGC 6535 | 2010 September 04 | $5 \times 400 \text{ s} + 253 \text{ s}$ | $F336W$ | WFC3/UVIS | 12008 | A. Kong |
| NGC 6752 | 2010 May 05 | $2 \times 500 \text{ s} + 30 \text{ s}$ | $F336W$ | WFC3/UVIS | 11729 | W. Freedman |
| NGC 6752 | 2011 May 18–September 04 | $12 \times 389 \text{ s} + 6 \times 10 \text{ s}$ | $F435W$ | WFC/ACS | 12254 | A. Reiners |

All the images have been corrected for the effect of poor charge transfer efficiency following Anderson & Bedin (2010). Photometry has been performed on each individual exposure by using the program `img2xym_wfc3uv`, which has been developed by Jay Anderson and is similar to the `img2xym_WFC` program (Anderson & King 2006), but optimized for UVIS/WFC3 data. For saturated very-bright stars the photometry was performed using the method developed by Gilliland (2004), which recovers the electrons that have bled into neighbouring pixels. We refer to Section 8.1 in Anderson et al. (2008) for details on the application of this method.

Stellar positions have been corrected for geometric distortion using the solution by Bellini, Anderson & Bedin (2011). Photometry has been calibrated to the Vega-mag system as in Bedin et al. (2005), by using the photometric zero-points provided by the WFC3/UVIS web page.¹ Stellar proper motions have been obtained as in Anderson & King (2003) and Piotto et al. (2012) by comparing the average stellar positions derived from the WFC3 images in the $F336W$ and $F438W$ bands with those from the catalogues by Anderson et al. (2008). We have included in the following analysis only stars that are cluster members according to their proper motions.

Since we are interested in high-precision photometry, we limited our study to relatively isolated stars with small astrometric uncertainties that are well fitted by the point spread function and selected by following the prescriptions given in Milone et al. (2012b). Finally, the photometry has been corrected for differential reddening that area crucial step in identifying multiple sequences from photometry. To do this, we have used the method by Milone et al. (2012b). In a nutshell, we derived a σ clipped fiducial line of the MS and the SGB of each cluster by putting a spline through the median value of colours and magnitude in progressively narrower magnitude intervals. We have then determined for each star the colour residuals of the closest 50 relatively bright and well-measured MS and SGB stars with respect to the fiducial line. To do this, we have excluded the target star from the calculation of its own differential reddening. We assumed as the differential reddening of each star the median value of such residuals measured along the reddening vector, while the uncertainty on the differential reddening has been derived as in Milone (2015).

3 MULTIPLE POPULATIONS ALONG THE RGB

In the next subsections, we explain how we measured the intrinsic $m_{F275W} - m_{F814W}$ and $C_{F275W, F336W, F438W}$ RGB width, and used these two quantities to construct the chromosome map of each cluster. We then continue our analysis by using these maps to identify the 1G and 2G stellar populations along the RGB.

3.1 The determination of the RGB colour and pseudo-colour width

The colour broadening of the RGB provides evidence for the presence and diversity of multiple stellar populations in GCs. Indeed, in a simple stellar population (made of chemically homogeneous and coeval stars) the observed RGB width is entirely due to observational errors, whereas the observed RGB width is much wider than expected from photometric errors if multiple stellar populations are present.

The procedure to estimate the RGB width in the m_{F814W} versus $m_{F275W} - m_{F814W}$ and $C_{F275W, F336W, F438W}$ plots is illustrated in Fig. 1

for the cluster NGC 6723, taken as an example; the procedure is based in part on the naive estimator (Silverman 1986). We started by dividing the RGB into a series of $F814W$ magnitude bins of size δm . The bins are defined over a grid of points separated by intervals of fixed magnitude ($s = \delta m/3$). The procedure is extended to the RGB region fainter than the HB level, where multiple sequences are more clearly visible.

For each bin in $F814W$, we calculated the value of the 4th and the 96th percentile of the $m_{F275W} - m_{F814W}$ and $C_{F275W, F336W, F438W}$ distributions, to which we associated the mean $F814W$ magnitude of RGB stars in each bin. The resulting envelope of the RGB is represented by the red and blue lines in Fig. 1. The smoothing has been performed by boxcar averaging, where each point has been replaced by the average of the three adjacent points. Due to the small number of upper RGB stars, above the HB level, the red and the blue envelopes in the region have been drawn by eye.

The observed RGB width, $W_{C_{F275W, F336W, F438W}}^{\text{obs}}$, has been derived as the difference between the $C_{F275W, F336W, F438W}$ index of the red and blue fiducial lines, calculated 2.0 $F814W$ magnitudes above the MS turnoff, as illustrated in panel (b1) of Fig. 1. The error associated to $W_{C_{F275W, F336W, F438W}}^{\text{obs}}$ has been determined by bootstrapping with replacements over the sample of RGB stars, then repeated 1000 times. The derived errors refer to one standard deviation of the bootstrapped measurements.

The observed RGB width is partly intrinsic and partly due to observational errors and limited statistics. The intrinsic RGB width, $W_{C_{F275W, F336W, F438W}}$, is calculated by subtracting in quadrature the errors affecting the observed width, which include both photometric errors and errors in the differential-reddening correction. The same procedure was adopted to measure the intrinsic $m_{F275W} - m_{F814W}$ RGB colour width, $W_{m_{F275W} - m_{F814W}}$, as illustrated in panel (a1) of Fig. 1. The results are listed in Table 2 and reveal that for all the analysed GCs, the RGB width is always significantly wider than expected from the errors alone, proving that all 57 GCs host multiple stellar populations.

3.2 The ‘chromosome maps’ of the multiple stellar populations

We now combine the pieces of information coming from both the m_{F814W} versus $m_{F275W} - m_{F814W}$ colour–magnitude diagram (CMD) and the m_{F814W} versus $C_{F275W, F336W, F438W}$ diagram to identify the multiple stellar populations in each GC. To this end, we have used the method illustrated in Fig. 1, analogous to the technique introduced in Papers II and III, and illustrated here for the RGB of NGC 6723. Briefly, we have ‘verticalized’ the two diagrams in such a way that the blue and the red fiducial lines translate into vertical lines. This is obtained by defining for each star:

$$\Delta_{F275W, F814W} = W_{F275W, F814W} \frac{X - X_{\text{fiducialR}}}{X_{\text{fiducialR}} - X_{\text{fiducialB}}} \quad (1)$$

$$\Delta_{C_{F275W, F336W, F438W}} = W_{C_{F275W, F336W, F438W}} \frac{Y_{\text{fiducialR}} - Y}{Y_{\text{fiducialR}} - Y_{\text{fiducialB}}}, \quad (2)$$

where $X = (m_{F275W} - m_{F814W})$ and $Y = C_{F275W, F336W, F438W}$ and ‘fiducial R’ and ‘fiducial B’ correspond to the red and the blue fiducial lines, respectively, as shown in panels (a2) and (b2) of Fig. 1.

Thus, $\Delta_{F275W, F814W} = 0$ and $\Delta_{C_{F275W, F336W, F438W}} = 0$ correspond to stars lying on the corresponding red fiducial line and the

¹ <http://www.stsci.edu/hst/acs/analysis/zeropoints/zpt.py>

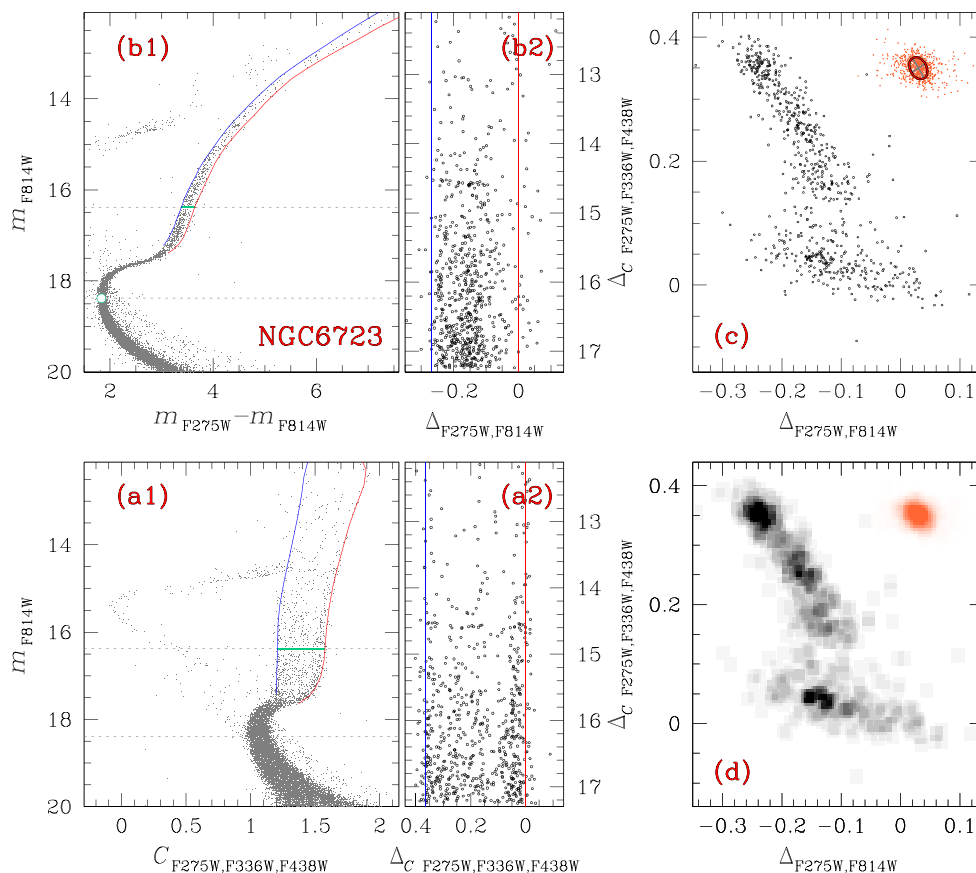


Figure 1. This figure illustrates the procedure to derive the $\Delta_{F275W, F336W, F438W}$ versus $\Delta_{F275W, F814W}$ pseudo-two-colour diagram (or ‘chromosome map’) for the prototypical cluster NGC 6723. Panels (a1) and (b1) show the m_{F814W} versus $C_{F275W, F336W, F438W}$ pseudo-CMD and the m_{F814W} versus $m_{F275W} - m_{F814W}$ CMD of NGC 6723. The aqua circle in panel (b1) marks the MS turnoff, whereas the two horizontal dotted lines in panels (a1) and (b1) are placed at the magnitude level of the MS turnoff and 2.0 $F814W$ mag above it. The blue and red lines mark the boundaries of the RGB, while the aqua segments in the panels (a1) and (b1) indicate the $m_{F275W} - m_{F814W}$ colour and the $C_{F275W, F336W, F438W}$ pseudo-colour separation between the two lines at 2.0 $F814W$ mag above the MS turnoff. The ‘verticalized’ m_{F814W} versus $\Delta_{C F275W, F336W, F438W}$ and m_{F814W} versus $\Delta_{F275W, F814W}$ diagrams for RGB stars are plotted in panels (a2) and (b2), respectively, where the red and blue vertical lines correspond to the RGB boundaries in panels (a1) and (b1) that translate into vertical lines in panel (a2) and (b2). The sample of RGB stars used to construct the chromosome map in panel (c) are those panels (a2) and (b2), where $\Delta_{F275W, F336W, F438W}$ and $\Delta_{C F275W, F814W}$ are defined in equations (1) and (2) as explained in the text. The orange points indicate the distribution of stars expected from observational errors only, while the red ellipses include the 68.27 per cent of the points. Panel (d) shows the Hess diagram for stars in panel (c).

Δ quantities represent the colour and pseudo-colour distance from such lines. The resulting $\Delta_{C F275W, F336W, F438W}$ versus $\Delta_{F275W, F814W}$ plot is shown in panels (c) and (d) and reveals the distinct stellar populations of NGC 6723.

Following the nomenclature introduced in Paper V, we will refer to plots such as those shown in panels (c) and (d) of Fig. 1 as the ‘chromosome map’ of a GC. The chromosome maps of all 57 GCs are presented in Section 4.

3.3 Distinguishing first- and second-generation stars

The chromosome map of NGC 6723 shown in panels (c) and (d) of Fig. 1 and in the left-hand panel of Fig. 2 reveals that cluster stars are distributed along two main, distinct groups that we name 1G and 2G and that correspond to the first and second generation of stars as defined in Paper V. It is indeed commonly believed that the multiple stellar populations phenomenon in GCs is the result of multiple events of star formation, where 2G stars form out of material processed by 1G stars (e.g. Decressin et al. 2007, Paper V, D’Antona et al. 2016, and references therein). Thus, in this paper we

will consider GC ‘multiple populations’ and ‘multiple generations’ as synonyms, as done in previous papers of this series.

We preliminarily identify 1G stars as those at nearly constant $\Delta_{C F275W, F336W, F438W}$ departing from the origin of the reference frame, located at $\Delta_{C F275W, F336W, F438W} = \Delta_{F275W, F814W} = 0$. As a consequence, 2G stars are identified as those in the steep branch reaching high values of $\Delta_{C F275W, F336W, F438W}$. A full justification of this choice is presented in Section 4.3, where 1G and 2G are chemically tagged, in analogy to what done in Paper II and Paper III.

The procedure to define a sample of bona fide 1G and 2G stars is illustrated in Fig. 2 for NGC 6723. The green line is a fit to the group of 1G stars and the angle between the green line and the dashed horizontal line is $\theta = 18^\circ$. We adopted this same value of θ for all the analysed clusters. The Δ_2 versus Δ_1 diagram shown in the middle panel of Fig. 2 has been obtained by rotating counterclockwise the left-hand panel diagram by an angle θ around the origin of the reference frame, and the black histogram plotted in the right-hand panel represents the normalized Δ_2 distribution of cluster stars. The orange points shown in the left-hand and middle

Table 2. Values of the RGB width and of the fraction of 1G stars with respect to the total number of analysed stars. We also indicate type-I and type-II clusters and the fraction of type-II stars with respect to the total number of analysed stars. The last two columns provide the number of analysed RGB stars and the ratio between the maximum radial distance from the cluster centre of the analysed stars (R_{\max}) and the cluster half-light radius (R_{hl}). For the type-II clusters, we provide in the second row the values of the RGB width obtained by excluding red-RGB stars ($W_{C\ F275W, F336W, F438W}^*$ and $W_{mF275W - mF814W}^*$).

| ID | $W_{C\ F275W, F336W, F438W}$ | $W_{mF275W - mF814W}$ | $W_{mF275W - mF814W}^{1G}$ | $W_{mF275W - mF814W}^{2G}$ | N_1/N_{TOT} | Type | $N_{\text{Type II}}/N_{\text{TOT}}$ | N_{stars} | R_{\max}/R_{hl} |
|----------|------------------------------|-----------------------|----------------------------|----------------------------|----------------------|------|-------------------------------------|--------------------|--------------------------|
| NGC 0104 | 0.369 ± 0.009 | 0.324 ± 0.019 | 0.216 ± 0.023 | 0.164 ± 0.008 | 0.175 ± 0.009 | I | 0 | 1853 | 0.56 |
| NGC 0288 | 0.276 ± 0.008 | 0.174 ± 0.009 | 0.075 ± 0.008 | 0.061 ± 0.014 | 0.542 ± 0.031 | I | 0 | 223 | 0.89 |
| NGC 0362 | 0.275 ± 0.005 | 0.192 ± 0.017 | 0.092 ± 0.012 | 0.103 ± 0.008 | 0.279 ± 0.015 | II | 0.075 ± 0.009 | 840 | 2.01 |
| | 0.271 ± 0.007 | 0.187 ± 0.013 | | | | | | | |
| NGC 1261 | 0.290 ± 0.010 | 0.203 ± 0.020 | 0.148 ± 0.025 | 0.072 ± 0.007 | 0.359 ± 0.016 | II | 0.038 ± 0.006 | 891 | 2.35 |
| | 0.281 ± 0.010 | 0.203 ± 0.020 | | | | | | | |
| NGC 1851 | 0.342 ± 0.005 | 0.206 ± 0.019 | 0.090 ± 0.010 | 0.093 ± 0.010 | 0.264 ± 0.015 | II | 0.030 ± 0.014 | 1022 | 3.00 |
| | 0.289 ± 0.010 | 0.182 ± 0.019 | | | | | | | |
| NGC 2298 | 0.243 ± 0.017 | 0.172 ± 0.021 | 0.139 ± 0.026 | 0.086 ± 0.014 | 0.370 ± 0.037 | I | 0 | 156 | 1.61 |
| NGC 2808 | 0.457 ± 0.009 | 0.518 ± 0.015 | 0.183 ± 0.017 | 0.335 ± 0.011 | 0.232 ± 0.014 | I | 0 | 2682 | 2.32 |
| NGC 3201 | 0.292 ± 0.016 | 0.211 ± 0.012 | 0.150 ± 0.040 | 0.111 ± 0.057 | 0.436 ± 0.036 | I | 0 | 169 | 0.52 |
| NGC 4590 | 0.132 ± 0.007 | 0.100 ± 0.005 | 0.065 ± 0.008 | 0.068 ± 0.007 | 0.381 ± 0.024 | I | 0 | 330 | 1.13 |
| NGC 4833 | 0.260 ± 0.008 | 0.208 ± 0.015 | 0.126 ± 0.012 | 0.134 ± 0.007 | 0.362 ± 0.025 | I | 0 | 401 | 0.73 |
| NGC 5024 | 0.209 ± 0.005 | 0.200 ± 0.014 | 0.169 ± 0.016 | 0.096 ± 0.008 | 0.328 ± 0.020 | I | 0 | 1081 | 1.35 |
| NGC 5053 | 0.102 ± 0.013 | 0.072 ± 0.009 | 0.049 ± 0.012 | 0.000 ± 0.007 | 0.544 ± 0.062 | I | 0 | 56 | 0.53 |
| NGC 5139 | 0.390 ± 0.010 | 1.090 ± 0.147 | 0.146 ± 0.011 | 0.260 ± 0.006 | 0.086 ± 0.010 | II | 0.640 ± 0.018 | 3084 | 0.50 |
| | 0.372 ± 0.010 | 0.254 ± 0.005 | | | | | | | |
| NGC 5272 | 0.279 ± 0.007 | 0.263 ± 0.012 | 0.244 ± 0.014 | 0.094 ± 0.006 | 0.305 ± 0.014 | I | 0 | 1177 | 0.83 |
| NGC 5286 | 0.303 ± 0.007 | 0.303 ± 0.021 | 0.146 ± 0.010 | 0.138 ± 0.007 | 0.342 ± 0.015 | II | 0.167 ± 0.010 | 1521 | 2.25 |
| | 0.292 ± 0.013 | 0.249 ± 0.014 | | | | | | | |
| NGC 5466 | 0.141 ± 0.016 | 0.108 ± 0.035 | 0.048 ± 0.029 | 0.042 ± 0.012 | 0.467 ± 0.063 | I | 0 | 62 | 0.67 |
| NGC 5897 | 0.149 ± 0.008 | 0.121 ± 0.014 | 0.081 ± 0.019 | 0.080 ± 0.012 | 0.547 ± 0.042 | I | 0 | 194 | 0.79 |
| NGC 5904 | 0.332 ± 0.013 | 0.219 ± 0.034 | 0.163 ± 0.033 | 0.105 ± 0.008 | 0.235 ± 0.013 | I | 0 | 965 | 0.90 |
| NGC 5927 | 0.422 ± 0.020 | 0.745 ± 0.065 | 0.631 ± 0.066 | 0.304 ± 0.037 | – | I | 0 | 583 | 1.52 |
| NGC 5986 | 0.294 ± 0.008 | 0.222 ± 0.007 | 0.070 ± 0.006 | 0.145 ± 0.007 | 0.246 ± 0.012 | I | 0 | 895 | 1.81 |
| NGC 6093 | 0.305 ± 0.015 | 0.246 ± 0.007 | 0.090 ± 0.008 | 0.159 ± 0.012 | 0.351 ± 0.029 | I | 0 | 668 | 2.52 |
| NGC 6101 | 0.140 ± 0.009 | 0.116 ± 0.012 | 0.063 ± 0.013 | 0.056 ± 0.008 | 0.654 ± 0.032 | I | 0 | 263 | 1.48 |
| NGC 6121 | 0.270 ± 0.007 | 0.161 ± 0.015 | 0.056 ± 0.045 | 0.099 ± 0.015 | 0.285 ± 0.037 | I | 0 | 135 | 0.39 |
| NGC 6144 | 0.210 ± 0.012 | 0.160 ± 0.012 | 0.121 ± 0.023 | 0.094 ± 0.008 | 0.444 ± 0.037 | I | 0 | 159 | 0.95 |
| NGC 6171 | 0.351 ± 0.017 | 0.220 ± 0.033 | 0.115 ± 0.020 | 0.104 ± 0.020 | 0.397 ± 0.031 | I | 0 | 245 | 0.90 |
| NGC 6205 | 0.291 ± 0.006 | 0.231 ± 0.008 | 0.096 ± 0.020 | 0.143 ± 0.006 | 0.184 ± 0.013 | I | 0 | 1198 | 1.05 |
| NGC 6218 | 0.274 ± 0.009 | 0.137 ± 0.009 | 0.073 ± 0.018 | 0.065 ± 0.015 | 0.400 ± 0.029 | I | 0 | 315 | 0.93 |
| NGC 6254 | 0.310 ± 0.007 | 0.236 ± 0.011 | 0.156 ± 0.020 | 0.100 ± 0.008 | 0.364 ± 0.028 | I | 0 | 488 | 0.86 |
| NGC 6304 | 0.320 ± 0.024 | 0.503 ± 0.053 | 0.371 ± 0.083 | 0.228 ± 0.028 | – | I | 0 | 602 | 1.13 |
| NGC 6341 | 0.177 ± 0.005 | 0.168 ± 0.009 | 0.078 ± 0.011 | 0.081 ± 0.003 | 0.304 ± 0.015 | I | 0 | 795 | 1.63 |
| NGC 6352 | 0.395 ± 0.015 | 0.332 ± 0.037 | 0.193 ± 0.053 | 0.171 ± 0.041 | 0.474 ± 0.035 | I | 0 | 221 | 0.76 |
| NGC 6362 | 0.292 ± 0.011 | 0.210 ± 0.048 | 0.093 ± 0.036 | 0.086 ± 0.010 | 0.574 ± 0.035 | I | 0 | 233 | 0.81 |
| NGC 6366 | 0.291 ± 0.064 | 0.318 ± 0.049 | 0.043 ± 0.075 | 0.131 ± 0.037 | 0.418 ± 0.045 | I | 0 | 72 | 0.51 |
| NGC 6388 | 0.494 ± 0.010 | 0.559 ± 0.027 | – | – | 0.245 ± 0.010 | II | 0.299 ± 0.016 | 1735 | 2.45 |
| NGC 6397 | 0.117 ± 0.023 | 0.077 ± 0.009 | 0.074 ± 0.011 | 0.031 ± 0.011 | 0.345 ± 0.036 | I | 0 | 111 | 0.55 |
| NGC 6441 | 0.512 ± 0.015 | 0.792 ± 0.025 | 0.283 ± 0.025 | 0.298 ± 0.017 | – | I | 0 | 1907 | 2.90 |
| NGC 6496 | 0.331 ± 0.038 | 0.311 ± 0.032 | 0.234 ± 0.033 | 0.125 ± 0.018 | 0.674 ± 0.035 | I | 0 | 196 | 1.40 |
| NGC 6535 | 0.142 ± 0.020 | 0.110 ± 0.067 | 0.088 ± 0.015 | 0.055 ± 0.041 | 0.536 ± 0.081 | I | 0 | 62 | 1.70 |
| NGC 6541 | 0.275 ± 0.007 | 0.214 ± 0.015 | 0.080 ± 0.009 | 0.103 ± 0.006 | 0.396 ± 0.020 | I | 0 | 692 | 1.56 |
| NGC 6584 | 0.221 ± 0.014 | 0.153 ± 0.030 | 0.133 ± 0.031 | 0.042 ± 0.010 | 0.451 ± 0.026 | I | 0 | 417 | 2.27 |
| NGC 6624 | 0.444 ± 0.015 | 0.436 ± 0.038 | 0.282 ± 0.040 | 0.196 ± 0.020 | 0.279 ± 0.020 | I | 0 | 594 | 1.87 |
| NGC 6637 | 0.367 ± 0.011 | 0.283 ± 0.016 | 0.151 ± 0.022 | 0.149 ± 0.011 | 0.425 ± 0.017 | I | 0 | 862 | 2.05 |
| NGC 6652 | 0.341 ± 0.014 | 0.277 ± 0.026 | 0.207 ± 0.027 | 0.089 ± 0.010 | 0.344 ± 0.026 | I | 0 | 340 | 3.09 |
| NGC 6656 | 0.293 ± 0.012 | 0.344 ± 0.019 | 0.152 ± 0.030 | 0.159 ± 0.018 | 0.274 ± 0.020 | II | 0.403 ± 0.021 | 557 | 0.51 |
| | 0.215 ± 0.010 | 0.234 ± 0.023 | | | | | | | |
| NGC 6681 | 0.309 ± 0.005 | 0.208 ± 0.009 | 0.060 ± 0.013 | 0.135 ± 0.007 | 0.234 ± 0.019 | I | 0 | 527 | 2.31 |
| NGC 6715 | 0.404 ± 0.009 | 0.388 ± 0.013 | 0.261 ± 0.016 | 0.190 ± 0.011 | 0.267 ± 0.012 | II | 0.046 ± 0.011 | 2358 | 2.08 |
| | 0.346 ± 0.012 | 0.349 ± 0.016 | | | | | | | |
| NGC 6717 | 0.293 ± 0.012 | 0.175 ± 0.070 | 0.029 ± 0.015 | 0.057 ± 0.018 | 0.637 ± 0.039 | I | 0 | 102 | 2.01 |
| NGC 6723 | 0.352 ± 0.006 | 0.268 ± 0.016 | 0.195 ± 0.020 | 0.128 ± 0.009 | 0.363 ± 0.017 | I | 0 | 695 | 1.05 |
| NGC 6752 | 0.320 ± 0.015 | 0.197 ± 0.010 | 0.100 ± 0.016 | 0.127 ± 0.008 | 0.294 ± 0.023 | I | 0 | 372 | 0.91 |
| NGC 6779 | 0.256 ± 0.007 | 0.203 ± 0.036 | 0.090 ± 0.039 | 0.102 ± 0.013 | 0.469 ± 0.041 | I | 0 | 420 | 1.29 |
| NGC 6809 | 0.211 ± 0.012 | 0.146 ± 0.006 | 0.086 ± 0.008 | 0.100 ± 0.010 | 0.311 ± 0.029 | I | 0 | 171 | 0.55 |
| NGC 6838 | 0.334 ± 0.014 | 0.236 ± 0.026 | 0.165 ± 0.025 | 0.046 ± 0.015 | 0.622 ± 0.038 | I | 0 | 132 | 0.88 |
| NGC 6934 | 0.312 ± 0.015 | 0.255 ± 0.021 | 0.123 ± 0.028 | 0.102 ± 0.016 | 0.326 ± 0.020 | II | 0.067 ± 0.010 | 606 | 2.30 |
| | 0.304 ± 0.013 | 0.237 ± 0.015 | | | | | | | |
| NGC 6981 | 0.240 ± 0.009 | 0.196 ± 0.019 | 0.142 ± 0.026 | 0.045 ± 0.018 | 0.542 ± 0.027 | I | 0 | 389 | 1.67 |
| NGC 7078 | 0.217 ± 0.003 | 0.215 ± 0.007 | 0.102 ± 0.007 | 0.106 ± 0.005 | 0.399 ± 0.019 | I | 0 | 1495 | 1.79 |
| NGC 7089 | 0.302 ± 0.009 | 0.309 ± 0.014 | 0.151 ± 0.022 | 0.166 ± 0.009 | 0.224 ± 0.014 | II | 0.043 ± 0.006 | 1296 | 1.47 |
| | 0.302 ± 0.009 | 0.309 ± 0.014 | | | | | | | |
| NGC 7099 | 0.140 ± 0.009 | 0.122 ± 0.017 | 0.000 ± 0.010 | 0.056 ± 0.009 | 0.380 ± 0.028 | I | 0 | 323 | 1.55 |

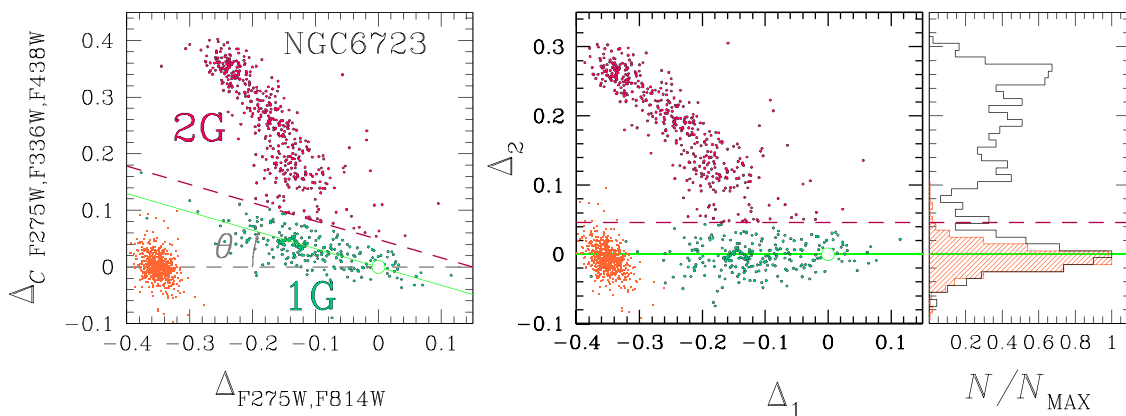


Figure 2. The figure illustrates the method used to identify the two samples of bona fide first-generation (1G) and second-generation (2G) stars in NGC 6723. The left-hand panel reproduces the $\Delta_{F275W, F336W, F438W}$ versus $\Delta_{F275W, F814W}$ diagram from Fig. 1. The green line through the origin of the frame is a fit to the sequence of candidate 1G stars and defines an angle $\theta = 18^\circ$ with respect to the horizontal line. The middle panel shows the Δ_2 versus Δ_1 plot where these new coordinates have been obtained by rotating counterclockwise by an angle θ the plot in the left-hand panel. The histogram in the right-hand panel shows the distributions of the Δ_2 values. The orange points in the left-hand and middle panels show the distribution of the observational errors and their Δ_2 distribution is represented by the shaded orange histogram in the right-hand panel. The dashed magenta lines separate the selected 1G and 2G stars, which are coloured aqua and magenta, respectively, in the left-hand and middle panels. See the text for details.

panels of Fig. 2 represent the expected distribution of the observational errors obtained by Monte Carlo simulations and have been plotted at the arbitrary position $\Delta_2 = 0$. The normalized histogram distribution of the Δ_2 errors is shown in orange in the right-hand panel of the figure. The magenta dashed line is then plotted at the Δ_2 level corresponding to the 3σ deviation from the mean of the error histogram, and the same line is also reported in the left-hand panel, after counter rotation.

We have then taken as bona fide 1G stars all those below the magenta dashed line, while the remaining stars are defined as 2G. 1G and 2G stars are coloured aqua and magenta, respectively, in the left-hand and middle panel of Fig. 2. We can already notice that the $\Delta_{F275W, F814W}$ and $\Delta_{CF275W, F336W, F438W}$ extension of both 1G and 2G stars in this cluster is significantly wider than expected from photometric errors alone, thus demonstrating that both 1G and 2G stars in the cluster are not chemically homogeneous. As we shall see, this is the case for the vast majority of our 57 GCs.

4 THE CHROMOSOME MAPS OF THE 57 GLOBULAR CLUSTERS

Figs 3–7 show a collection of the chromosome maps for all 57 GCs studied in this paper. GCs are roughly sorted in order of decreasing metallicity, from the most metal rich (NGC 6624, $[\text{Fe}/\text{H}] = -0.44$, Fig. 3) to the most metal poor (NGC 7078, $[\text{Fe}/\text{H}] = -2.37$, Fig. 7).

4.1 Classifying clusters in two main types

In most maps, it is possible to easily identify the two main groups of 1G and 2G stars as it was the case for NGC 6723 (see Fig. 2). The magenta dashed lines superimposed on each panel of Figs 3–7 have been derived as described in Section 4.2 and have been used to identify the two groups of bona fide 1G and 2G stars of each cluster. Clusters for which the map allows the 1G/2G distinction as described for NGC 6723 are called here type-I clusters. However, the extension of the 1G group of stars and its separation from the 2G group are quite ambiguous in some clusters, and eventually a distinction between 1G and 2G groups is no longer possible, at

least with the present photometric accuracy. This is the case for the three clusters NGC 5927, NGC 6304, and NGC 6441. The 1G/2G separation may still be possible using other passbands, such as in the case of NGC 6441 (Bellini et al. 2013).

Finally, several other clusters exhibit more complex chromosome maps, with an additional 2G sequence (e.g. NGC 1851) or even what appears to be a split of both 1G and 2G sequences (e.g. NGC 6934). Stars in these additional sequences are coloured in red in the chromosome maps. These are the clusters that define the type II and, besides the mentioned NGC 1851 and NGC 6934, this group includes NGC 362, NGC 1261, NGC 5286, NGC 6388, NGC 6656, NGC 6715, NGC 7089, and the famous ω Cen which, not surprisingly, has the most complex map of them all. Noticeably, in order to derive the red and blue fiducial lines that are used to determine the chromosome map of type-II GCs (see Fig. 1), we used only blue-RGB stars. Type-II clusters deserve a dedicated analysis, which is presented in Section 5.

As illustrated by Figs 3–7, the chromosome maps of type-I GC exhibit a great deal of variety. In particular, the $\Delta_{CF275W, F336W, F438W}$ and $\Delta_{F275W, F814W}$ extensions differ from one cluster to another, and in several clusters distinct clumps are clearly visible within the 1G and/or the 2G sequences. This is the case of NGC 2808 where at least five distinct subpopulations can be identified, as already illustrated in Paper III. The detailed study of substructures within the 1G and 2G sequences is not further developed in this paper.

Among type-I clusters, quite surprising is the case of NGC 6441, often considered a twin cluster of NGC 6388, since both are metal-rich clusters with an extended blue HB (e.g. Rich et al. 1997; Bellini et al. 2013, and references therein). Yet, their chromosome maps are radically different, with the type-II NGC 6388 exhibiting a very complex map whereas the type-I NGC 6441 shows a unique sequence where it is not even possible to distinguish between 1G and 2G stars. Similarly, we note significant difference between the chromosome map of the second-parameter pair cluster NGC 6205 (M 13) and NGC 5272 (M 3), with the latter hosting a very extended 1G. First- and second-generation stars in the other famous second-parameter pair, NGC 288 NGC 362, share a similar distribution in the corresponding chromosome maps. Intriguingly,

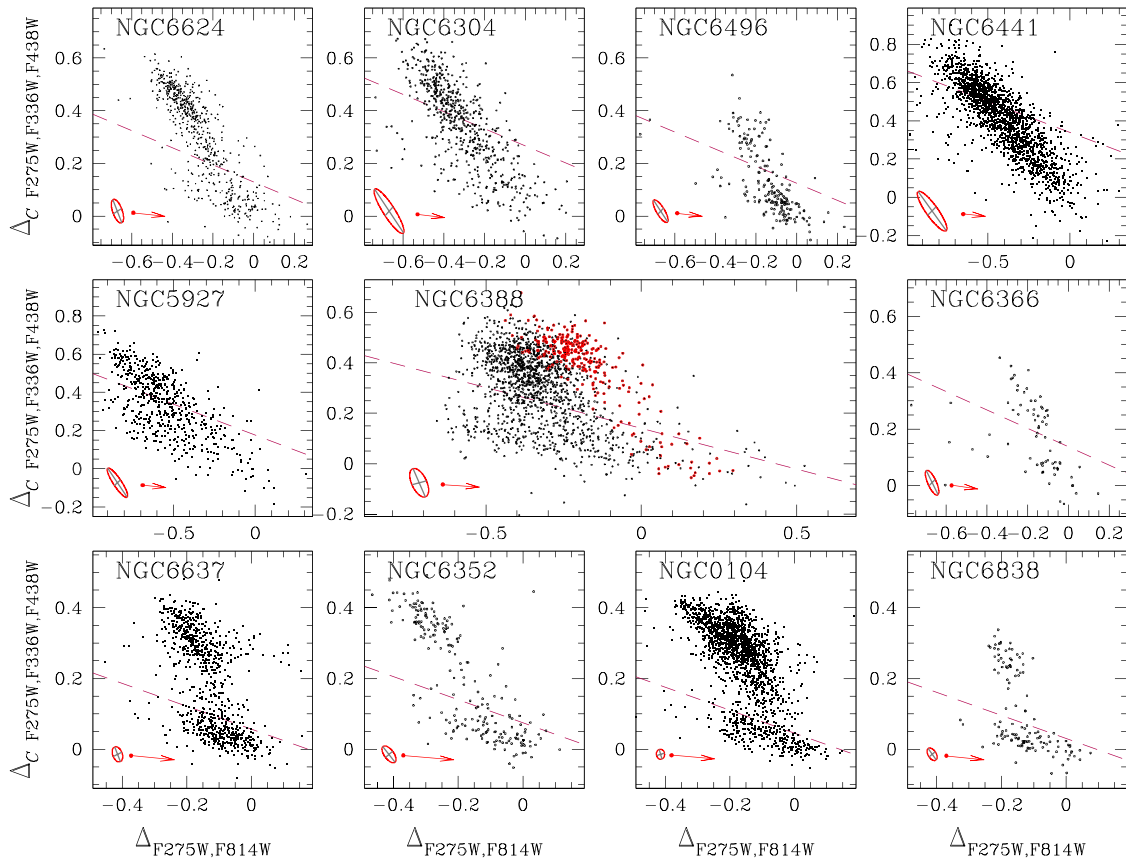


Figure 3. $\Delta_{CF275W, F336W, F438W}$ versus $\Delta_{F275W, F814W}$ diagrams, or chromosome maps, for RGB stars in 11 GCs. Namely NGC 6624, NGC 6304, NGC 6496, NGC 6441, NGC 5927, NGC 6388, NGC 6366, NGC 6637, NGC 6352, NGC 104 (47 Tucanae), and NGC 6838 (M 71). Clusters are approximately sorted according to their metallicity, from the most metal rich, to the most metal poor. The ellipses are indicative of the observational errors and include 68.27 per cent of the simulated stars. The magenta dashed line is used to separate bona fide 1G from 2G stars and has been determined as in Section 4.2. Red points indicate red-*RGB* stars and will be selected and discussed in Section 5, while the arrows indicate the reddening vector and correspond to a reddening variation of $\Delta E(B - V) = 0.05$. Note, however, that all these plots are constructed using photometric data corrected for differential reddening.

NGC 362 hosts a poorly populated red *RGB*, which is not present in NGC 288.

4.2 The fraction of 1G stars

The procedure to estimate the fraction of 1G stars with respect to the total number of studied *RGB* stars (N_{TOT}) is illustrated in the upper panels of Fig. 8 for NGC 6723, where we reproduce the Δ_2 versus Δ_1 plot shown in Fig. 2, now having coloured 1G and 2G stars aqua and magenta, respectively. The corresponding histogram distribution of Δ_2 is plotted in the upper-right panel of Fig. 8. The Gaussian fit to the distribution of bona fide 1G stars selected in Section 3.2 is represented by the red continuous line. The fraction of 1G stars (N_1/N_{TOT}) has been derived as the ratio between the area under the Gaussian and the total number of *RGB* stars in the chromosome map.

The middle panels of Fig. 8 illustrate the procedure described above, now applied to NGC 6205 where the separation between 1G and 2G stars is much less evident than for NGC 6723. NGC 6205 is the most uncertain case for a cluster that we classified as type I. The lower panels of Fig. 8 show the case for NGC 6441, where there is no appreciable separation between 1G and 2G stars, making NGC 6441 a typical example of a type-I cluster for which we did not attempt to estimate the fraction of 1G stars.

The derived fractions of 1G stars are listed in Table 2 which also provides the total number of *RGB* stars included in the chromosome map and the ratio between the maximum radius of the analysed stars and the cluster half-light radius. Radial gradients in the distribution of the 1G and 2G stars are indeed known to exist in some clusters (e.g. Sollima et al. 2007; Bellini et al. 2009, 2013; Johnson & Pilachowski 2010; Milone et al. 2012b; Cordero et al. 2014), hence this ratio provides a rough indication of the relative number of stars within the analysed field of view with respect to the entire cluster stellar population.

A visual inspection of the maps shown in Figs 3–7 reveals that the $\Delta_{F275W, F814W}$ extension of 1G and 2G stars may dramatically differ from one cluster to another. For example, in NGC 6205 and NGC 6752 the second generation is significantly more extended than the first one, while in NGC 5024 and NGC 5272 1G and 2G stars have a similar extension.

In order to quantify the $\Delta_{F275W, F814W}$ extension of 1G and 2G stars, we determined the width of the 1(2)G, $W_{F275W, F814W}^{obs, 1(2)G}$, as the difference between the 90th and the 10th percentile of the $\Delta_{F275W, F814W}$ distribution of 1(2)G stars. The intrinsic width has been estimated by subtracting the colour errors in quadrature (including errors associated with the differential reddening corrections). The values of $W_{F275W, F814W}^{1(2)G}$ are also listed in Table 2.

As already noted, the fact that $W_{F275W, F814W}^{1(2)G}$ is significantly larger than zero in most GCs, (i.e. the observed 1G and 2G widths are

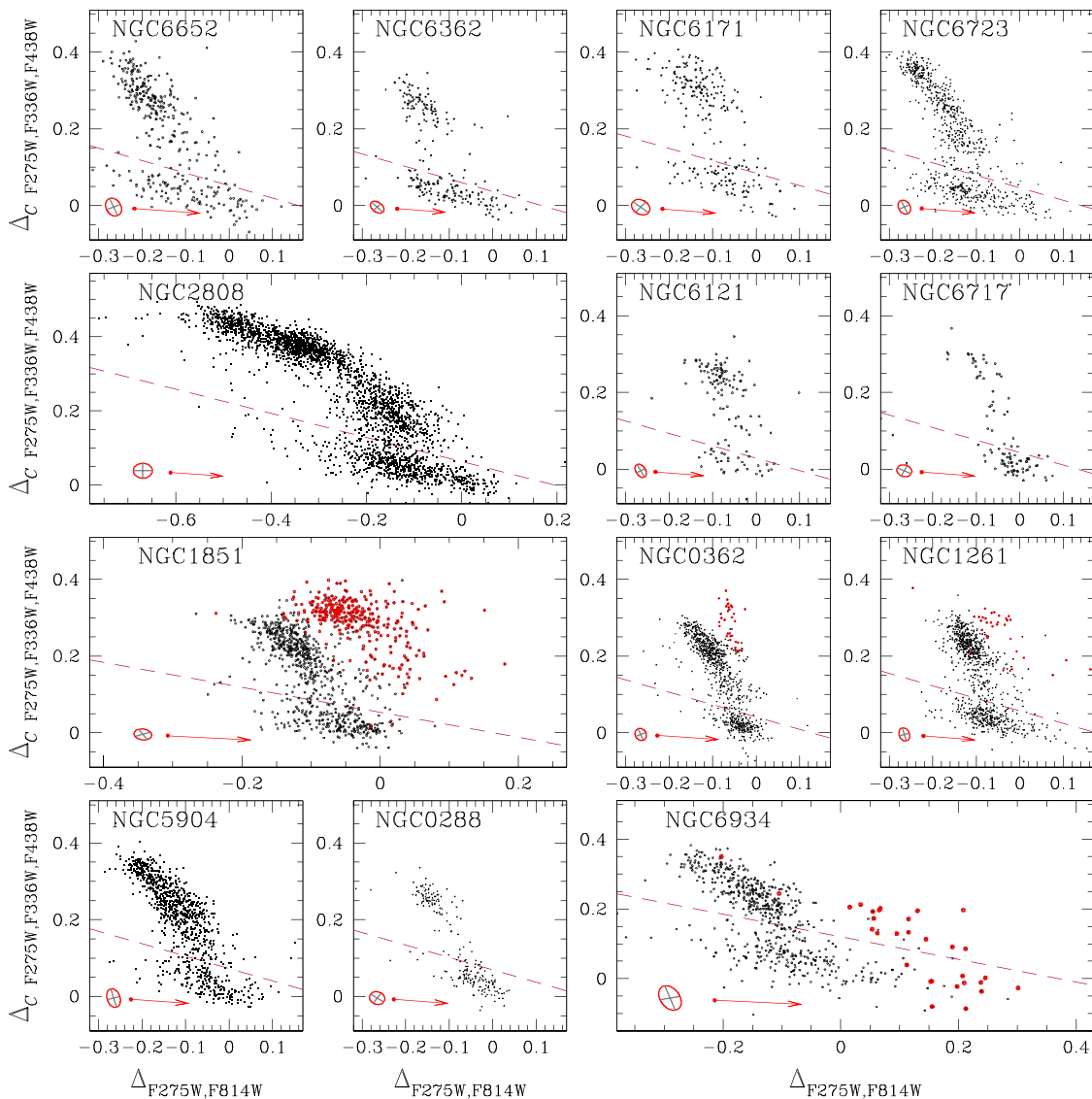


Figure 4. As in Fig. 3, but for NGC 6652, NGC 6362, NGC 6171 (M 107), NGC 6723, NGC 2808, NGC 6121 (M 4), NGC 6717, NGC 1851, NGC 362, NGC 1261, NGC 5904 (M 5), NGC 288, and NGC 6934.

larger than measurement errors) demonstrates that neither 1G nor 2G are consistent with a simple stellar population. This raises a new fundamental question: what are the chemical differences within the 1G population of a GC?

4.3 The chemical composition of multiple stellar populations

The chemical characterization of the multiple populations identified on the chromosome maps is a key step to justify our identification of 1G and 2G stars as belonging to the first and the second generation and an indispensable tool to understand their origin. For this purpose, the spectroscopic analysis of some stars included in our chromosome maps is needed. At present, we can rely only on existing data but additional extensive spectroscopic surveys are needed to shed further light on our photometric data.

To illustrate the case, in Fig. 9 we focus on NGC 6121 as a prototype of a type-I cluster. Multiple stellar populations in NGC 6121 have been widely studied, both photometrically (e.g. Marino et al. 2008; Milone et al. 2014; Nardiello et al. 2015b) and spectroscop-

ically (e.g. Ivans et al. 1999; Marino et al. 2008, 2011; Carretta et al. 2009, 2013). From Marino et al. (2008), chemical analysis is available for 11 stars in common with our WFC3/UVIS sample of RGB stars. Panel (b) of Fig. 9 shows the sodium–oxygen anticorrelation, where some stars are oxygen rich and sodium poor, hence with primordial chemical composition, while others are enhanced in sodium and depleted in oxygen. These stars are shown, respectively, with aqua and magenta filled circles in panels (a) and (b) of Fig. 9, showing that those we have called 1G stars have indeed primordial chemical composition, while 2G stars are Na rich and O poor. No significant differences in iron content appear to exist among 1G and 2G stars in NGC 6121. In Papers II and III, we performed a similar chemical tagging for NGC 7089 and for NGC 2808, by comparing the chromosome map of these clusters with the light-element abundances from Yong et al. (2014) and Carretta et al. (2006), respectively.

The chemical tagging of stars identified on the chromosome maps is clearly very limited at this time, but it could be greatly expanded by future spectroscopic observations targeting stars selected on the

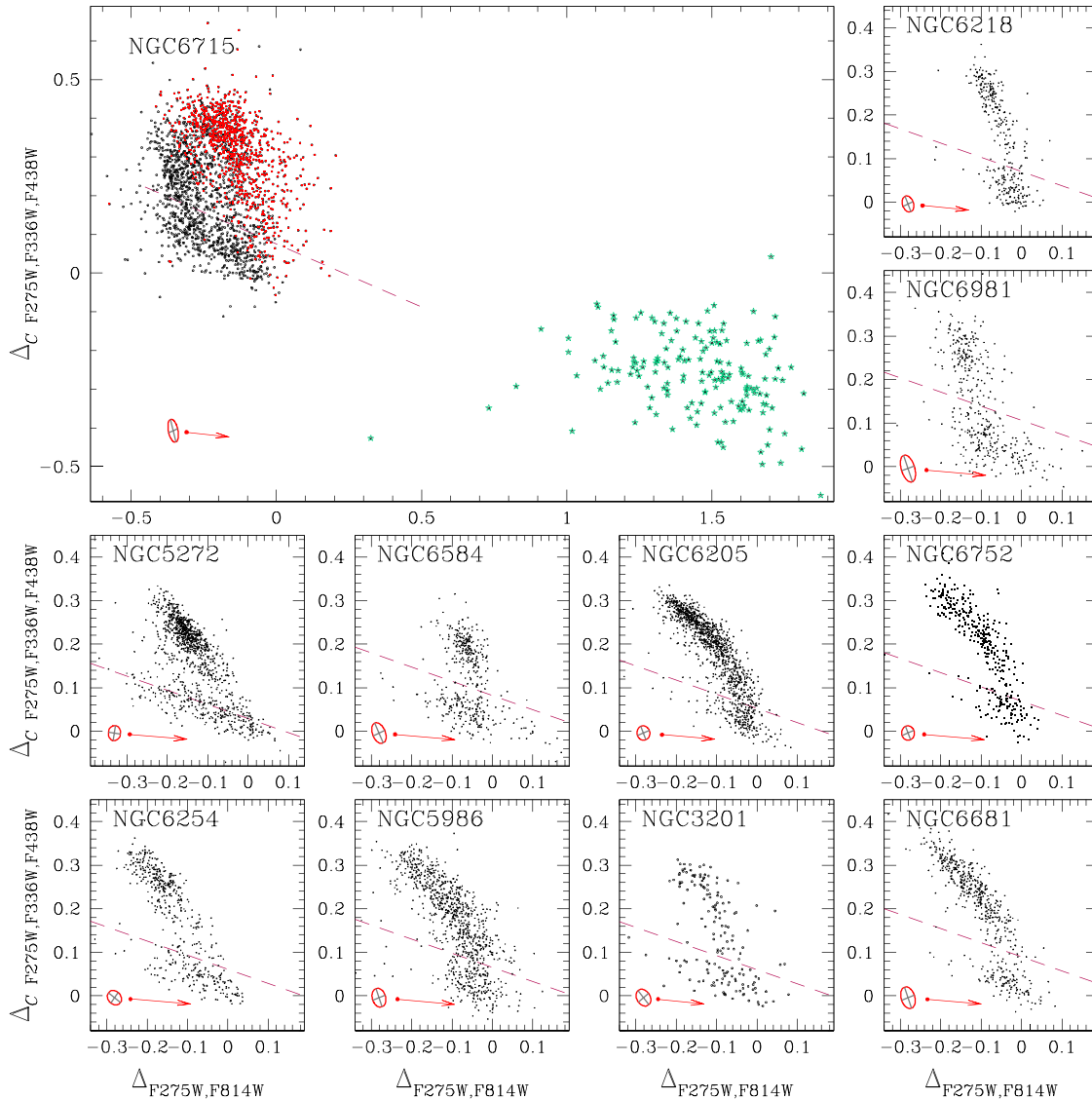


Figure 5. As in Fig. 3, but for the stellar system formed by NGC 6715 (M 54), and for NGC 6218 (M 12), NGC 6981 (M 72), NGC 5272 (M 3), NGC 6584, NGC 6205 (M 13), NGC 6752, NGC 6254 (M 10), NGC 5986, NGC 3201, and NGC 6681 (M 70). The aqua-starred symbols in the map of M 54 indicate stars of the metal-rich population in the core of the Sagittarius dwarf galaxy, to which M54 belongs.

chromosome maps illustrated in this paper. The other panels in Fig. 9 refer to the type-II GC NGC 5286 and will be used in the next section dedicated to type-II clusters.

5 GLOBULAR CLUSTERS OF TYPE II

In this section, we present additional evidence to further explore and characterize the stellar-population content of type II GCs, the most complex ones. A visual inspection of the chromosome map of NGC 1851 (Fig. 4) reveals that the map itself appears to be split, with two 2G sequences running vaguely parallel to each other, and a hint of a second 1G sequence as well. To better understand the origin of such a complex pattern, in Fig. 10 we show a collection of CMDs for NGC 1851. The CMD in the upper panel reveals that the SGB is clearly split into a bright and faint SGB (red points in the insert for the latter) which are connected to the blue and the red RGB, respectively. The RGB splitting was first noticed by

Han et al. (2009) using ground-based U versus $U - I$ photometry. The red- RGB stars have been coloured red in the upper panel of Fig. 10.

We used the same colours to represent the sample of selected faint-SGB stars in the m_{F438W} versus $m_{F438W} - m_{F814W}$, m_{F606W} versus $m_{F606W} - m_{F814W}$, and m_{F275W} versus $m_{F275W} - m_{F814W}$ CMDs, plotted in the lower panels of Fig. 10. These CMDs not only demonstrate that the split SGB of NGC 1851 is real, but also show that the faint SGB is visible also in CMDs made with optical filters, like m_{F606W} versus $m_{F606W} - m_{F814W}$, where stellar colours and luminosities are not significantly affected by light-element abundance variations (see also Milone et al. 2008). This indicates that faint-SGB stars are either enhanced in their C+N+O overall abundance, or are older than stars on the bright SGB by $\sim 1-2$ Gyr (Cassisi et al. 2008; Ventura et al. 2009; Marino et al. 2011). We emphasize that all type-II clusters exhibit either split or multimodal SGBs when observed in both ultraviolet and optical filters, in contrast to type-I GCs, where multiple populations along the SGB are visible only in

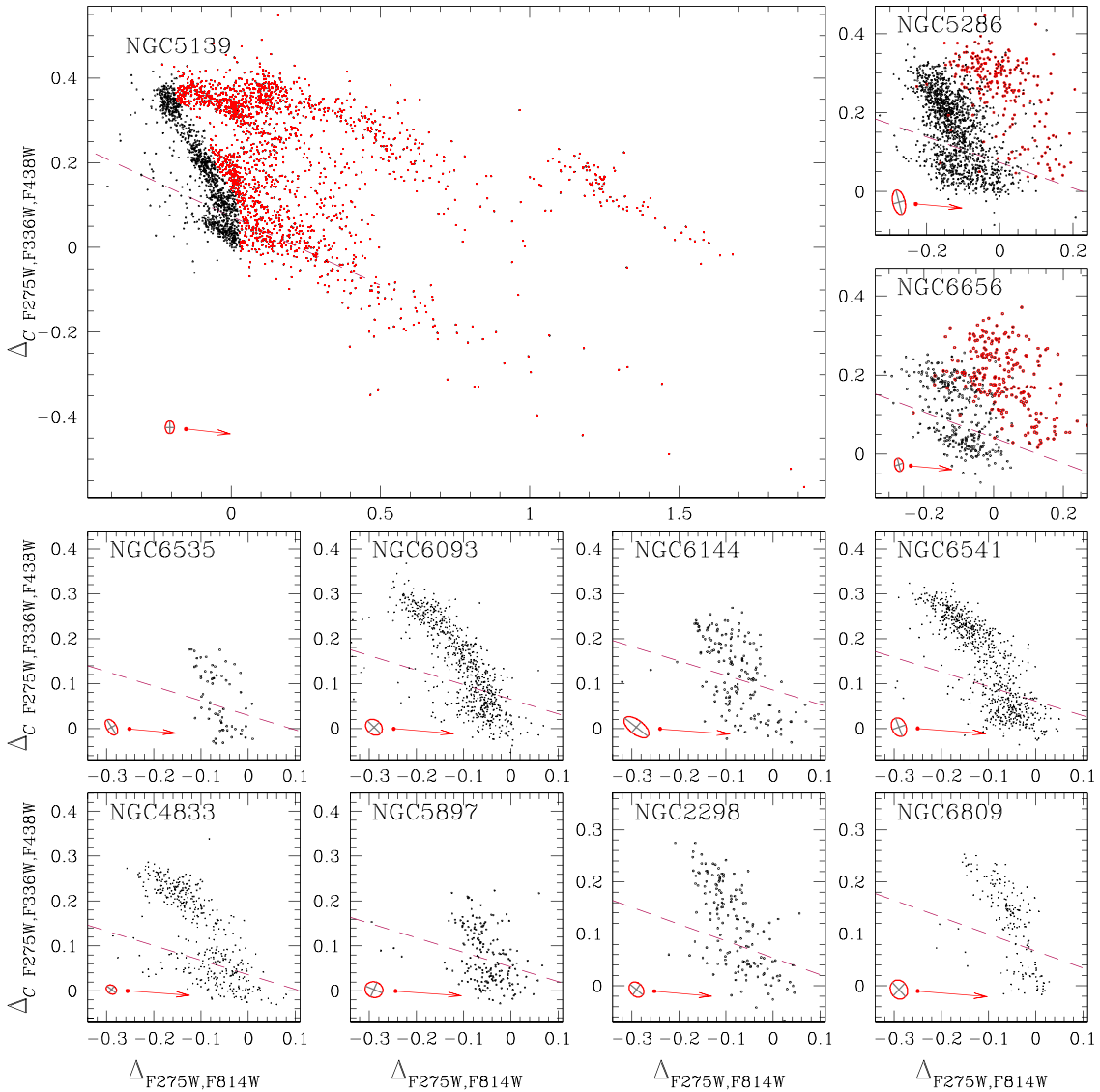


Figure 6. As in Fig. 3, but for NGC 5139 (ω Centauri), NGC 5286, and NGC 6656 (M 22), NGC 6535, NGC 6093 (M 80), NGC 6144, NGC 6541, NGC 4833, NGC 5897, NGC 2298, and NGC 6809 (M 55).

CMDs that include ultraviolet bands (Milone et al. 2008; Marino et al. 2009; Piotto et al. 2012).

A collection of CMDs for other type-II clusters (namely, NGC 362, NGC 1261, NGC 5139, NGC 5286, NGC 6656, NGC 6715, NGC 6093, and NGC 7078) is provided in Figs 11–18. Every CMD shows the existence of a faint SGB that evolves into a red RGB in the m_{F336W} versus $m_{F336W} - m_{F814W}$ CMD. As shown in Fig. 16, the faint-SGB–RGB connection is unclear for NGC 6388 where the RGB split is visible only for stars brighter than $m_{F336W} \lesssim 20.75$. Another possible exception is 47 Tucanae, in which there is no clear connection between multiple populations along the faint SGB and the RGB (Milone et al. 2012b). The red-RGB stars identified in Figs 11–18 are coloured in red in the chromosome maps shown in Figs 3–7. The fact that red-RGB stars are clearly separated from the majority of cluster members in the chromosome maps demonstrates that the $\Delta_{CF275W, F336W, F438W}$ versus $\Delta_{F275W, F814W}$ diagram is an efficient tool to identify GCs with multiple SGBs in the optical bands.

The fraction of red-RGB stars with respect to the total number of analysed RGB stars differs significantly from one type-II cluster to another, and ranges from a minimum of ~ 4 per cent for NGC 1261 and NGC 7089 to a maximum of ~ 46 per cent and ~ 64 per cent for NGC 6715 and NGC 5139 (ω Centauri), coming almost to dominate the cluster. Given its complexity, the special case of ω Centauri requires a somewhat more elaborate procedure for the measurement of the RGB width and the construction of its chromosome map, which is illustrated in Appendix A.

For type-II GCs, we have determined the RGB widths $W_{CF275W, F336W, F438W}$ and $W_{m_{F275W} - m_{F814W}}$ as described in Section 3.2 for NGC 6723, but both by using only stars belonging to the blue RGB and by using all the RGB stars. The latter quantities are called $W_{CF275W, F336W, F438W}^*$ and $W_{m_{F275W} - m_{F814W}}^*$. Both W and W^* width values are reported in Table 2, with W^* values given in a second row for each of the type-II clusters.

In order to illustrate the chemical tagging of multiple populations in type-II clusters, we use NGC 5286 as a prototype. In panel (c)

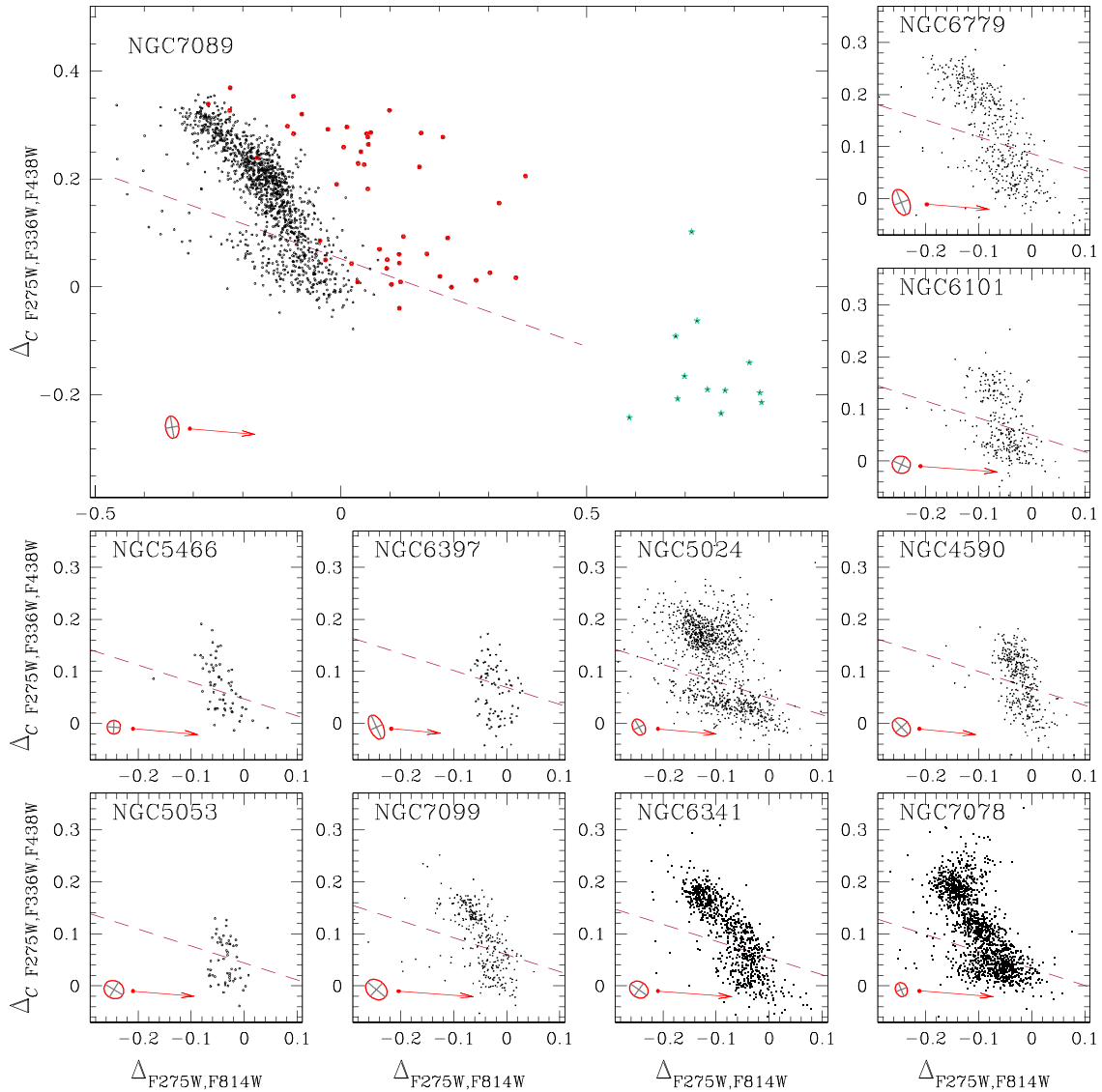


Figure 7. As in Fig. 3, but for NGC 7089 (M 2), NGC 6779 (M 56), NGC 6101, NGC 5466, NGC 6397, NGC 5024, NGC 4590, NGC 5053, NGC 7099 (M 30), NGC 6341 (M 92), and NGC 7078 (M 15). Stars in the most metal-rich population of NGC 7089 are represented with aqua-starred symbols.

of Fig. 9, red-RGB stars of this cluster are coloured red whereas large black filled circles and red triangles are used for those stars for which Marino et al. (2015) have measured their content of iron and s-process-elements, as shown in panel (d). Stars with low iron and barium belong to the 1G and 2G of the blue RGB, coloured in black, while the stars enhanced in [Fe/H] and [Ba/Fe] populate the red RGB.

In panels (a) and (c) of Fig. 19 we show separately the stars of the blue and the red RGBs of NGC 5286, and compare the position of stars in the chromosome map and in the Na–O plot, in close analogy with what was previously done for NGC 6121. We find that both RGBs host 1G stars with primordial oxygen and sodium abundance, and 2G stars enriched in sodium and depleted in oxygen, as shown in panels (b) and (d). In Panel (c), we indicate 1G and 2G stars of the red RGB as 1G,r and 2G,r, respectively. This finding is consistent with the conclusion by Marino et al. (2015) that both the group of barium-rich and barium-poor stars of NGC 5286 exhibit their own Na–O anticorrelation. In Paper II, we have reached a similar conclusion for NGC 7089, using the abundances of light

elements, s-process elements, and [Fe/H] from Yong et al. (2014). NGC 7089 hosts a population of stars highly enhanced in iron with respect to the majority of cluster members. Stars in the extreme population of NGC 7089 and the metal-rich stars in the core of the Sagittarius dwarf galaxy which are within the WFC3/UVIS images of NGC 6715 have been represented with aqua-starred symbols in the corresponding chromosome maps.

One intriguing discovery of the last decade is that a small but still increasing number of GCs host two or more distinct groups of stars with different content of iron and s-process elements (Johnson et al. 2015; Marino et al. 2015; Yong, Da Costa & Norris 2016, and references therein), while the majority of clusters have in general homogeneous abundances of s-process elements and metallicity. Moreover, the s-process-rich stars are also iron rich and, in the cases of NGC 6656, NGC 1851, and ω Centauri, these stars are also enhanced in their overall C+N+O abundance (Yong et al. 2009, 2014; Marino et al. 2011, 2012, 2015; Villanova et al. 2014).

The chemical tagging of multiple populations is still quite fragmentary, especially for type-II clusters. However, all the available

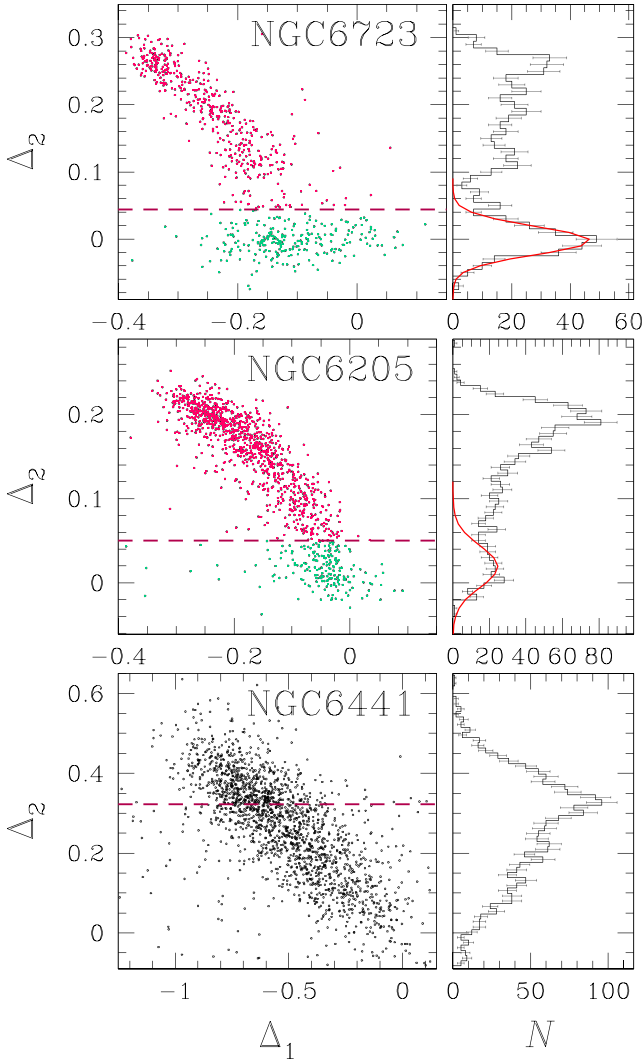


Figure 8. This figure exemplifies the procedure to estimate the fraction of 1G stars with respect to the total number of RGB stars, for NGC 6723 (upper panels) and NGC 6205 (middle panels). The left-hand panels show the Δ_2 versus Δ_1 diagrams presented in Section 4.2, where the pre-selected 1G and 2G stars are coloured aqua and magenta, respectively. The histogram in the right-hand panels show the distributions of the Δ_2 values. The red lines superimposed on the histograms of NGC 6723 and NGC 6205 are the best-fitting Gaussians of the 1G peak of the histogram. The fraction of 1G stars is then calculated as the ratio of the area of the Gaussian over that of the whole histogram. Lower panels show the case of NGC 6441, a type-I cluster, for which no clear distinction can be made between 1G and 2G stars and, correspondingly, we did not estimate the fraction of 1G stars. See the text for details.

evidence indicates that stars in the faint SGB and red RGB are enhanced in global C+N+O content, in iron and in s-process elements. We conclude that type-II clusters differ from type I ones in three aspects: the SGB of type-II GCs splits in optical bands, they host multiple 1G and/or 2G sequences in the chromosome maps and they show a wide composition range in heavy elements. Of course, these three characteristics ought to be physically connected to each other. To the best of our current understanding, each of these three properties, separately, is sufficient to identify as such a type-II cluster. We refer the reader to paper by Marino et al. (2015) and reference therein for further discussion on the chemical composition of type-II GCs.

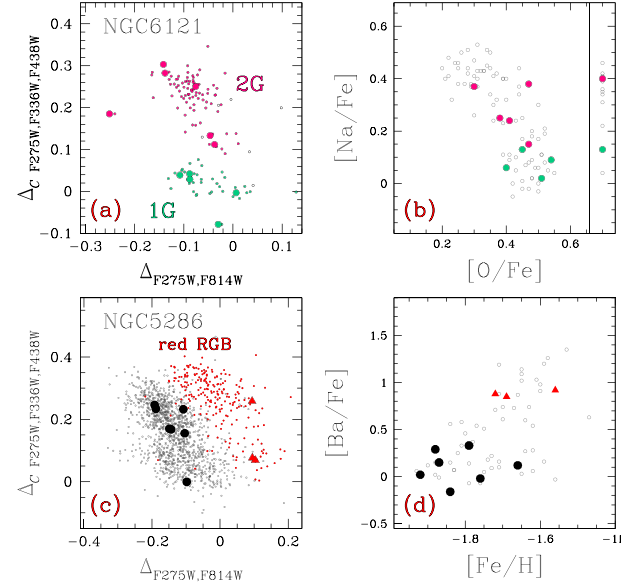


Figure 9. Panel (a) shows the chromosome map of RGB stars in the type I cluster NGC 6121, where we have coloured aqua and magenta 1G and 2G stars, respectively. Large aqua and magenta dots indicate 1G and 2G stars studied spectroscopically by Marino et al. (2008), and whose [Na/Fe] versus [O/Fe] anticorrelation is shown in panel (b) using the same symbols. Stars for which an oxygen abundance determination is not available are plotted on the right side of the vertical line in this and in similar panels. The chromosome map of the type II NGC 5286 is shown in panel (c), where red-RGB stars are coloured red and black point are used for the remaining RGB stars. Large black circles and red triangles indicate those stars studied spectroscopically by Marino et al. (2015), and whose [Ba/Fe] versus [Fe/H] plot is shown in panel (d).

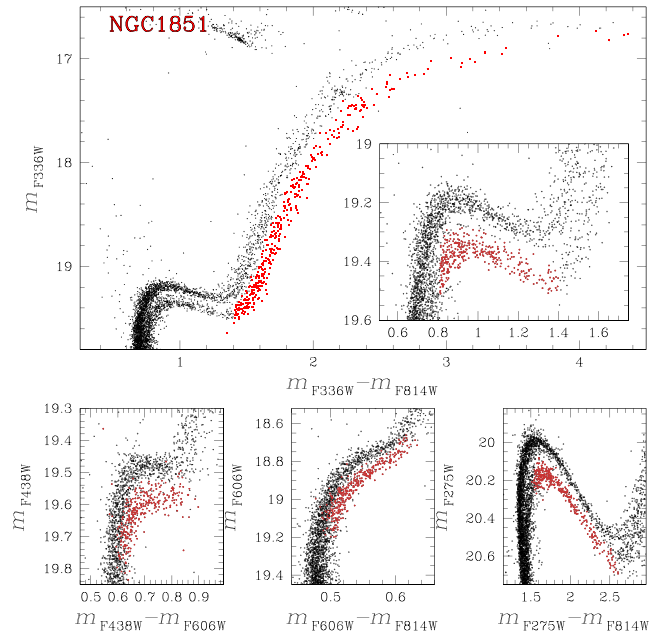


Figure 10. Upper panel: the m_{F336W} versus $m_{F336W} - m_{F814W}$ CMD of NGC 1851 with red-RGB stars coloured red. The inset shows a zoomed-in view around the SGB. Lower panels: m_{F438W} versus $m_{F438W} - m_{F606W}$ (left), m_{F606W} versus $m_{F606W} - m_{F814W}$ (middle), and m_{F275W} versus $m_{F275W} - m_{F814W}$ (right) CMDs around the SGB. The sample of faint SGB stars selected from the CMD in the insert of the upper panel are coloured red in these panels.

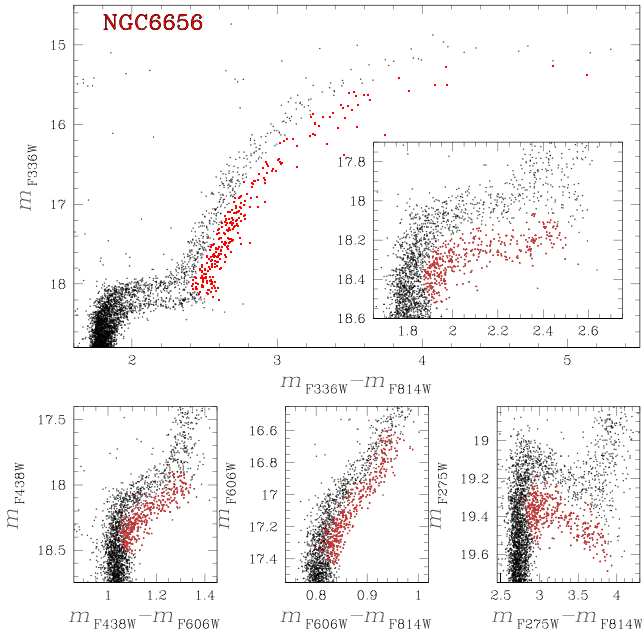


Figure 11. As in Fig. 10 but for NGC 6656.

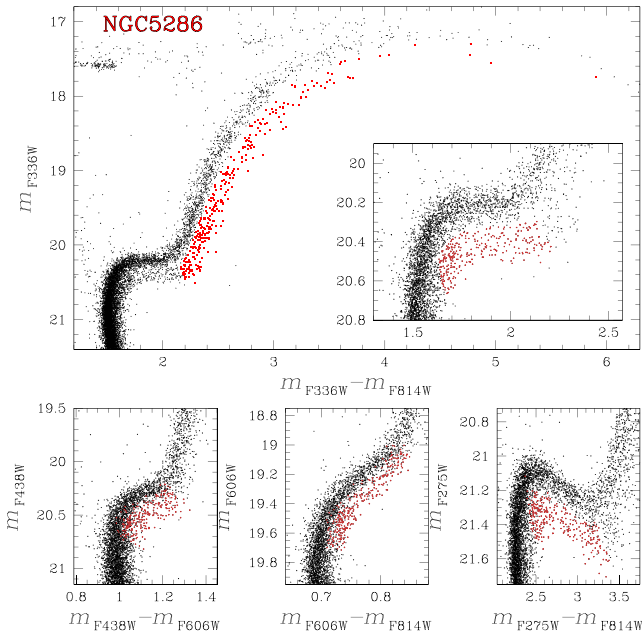


Figure 12. As in Fig. 10 but for NGC 5286.

6 UNIVARIATE RELATIONS BETWEEN MULTIPLE POPULATIONS AND GLOBAL CLUSTER PARAMETERS

In this Section, we investigate the correlation between the $W_{CF275W, F336W, F438W}$ and $W_{F275W, F814W}$ RGB widths and the 1G fraction, as determined in Section 3, and the global parameters of the host GCs. Such global GC parameters include: metallicity ($[Fe/H]$), absolute visual magnitude (M_V), central velocity dispersion (σ_V), ellipticity (ϵ), central concentration (c), core relaxation time (τ_c), half-mass relaxation time (τ_{hm}), central stellar density (ρ_0), central surface brightness (μ_V), reddening ($E(B - V)$), and Galactocentric distance (R_{GC}). All these quantities are taken from the 2010 edition of the Harris (1996) catalogue.

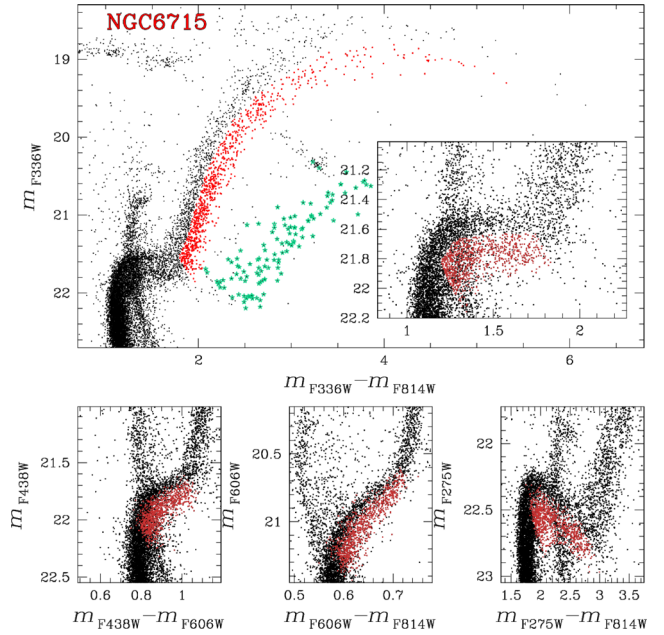


Figure 13. As in Fig. 10 but for NGC 6715. This cluster (also known as M54) sits in the core of the Sagittarius dwarf galaxy, and the CMD in the upper panel shows stars of both the cluster and the core of this galaxy. In particular, the extremely red RGB of the metal-rich population of Sagittarius' core is recognizable just to the left of the inset (aqua-starred symbols). These Sagittarius RGB stars are coloured aqua in the chromosome map of NGC 6715 shown in Fig. 5.

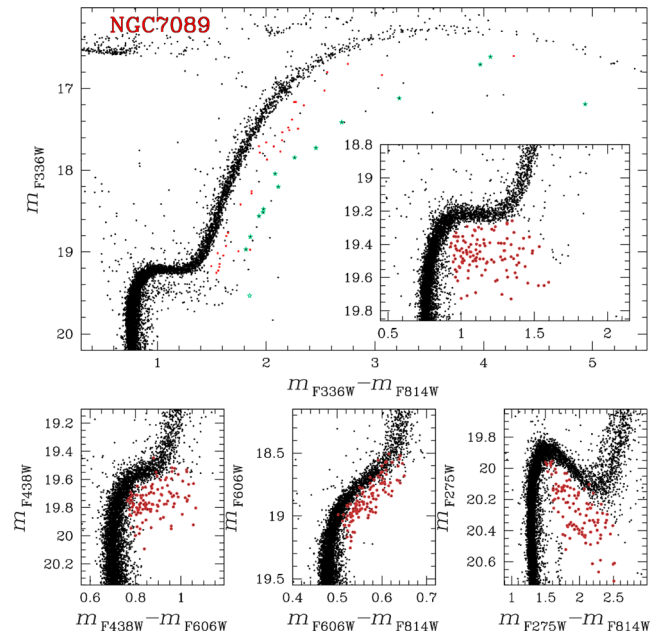


Figure 14. As in Fig. 10 but for NGC 7089. The stars in the most iron-rich RGB are represented with aqua stars.

The cluster masses have been taken from McLaughlin & van der Marel (2005) for 44 of the GCs studied in this paper. The results of our paper are based on the masses obtained by fitting the models by Wilson (1975) on the profiles of 63 Galactic GCs by Trager, King & Djorgovski (1995). The fraction of binary stars in GCs has been taken from Milone et al. (2012a), as measured within the cluster

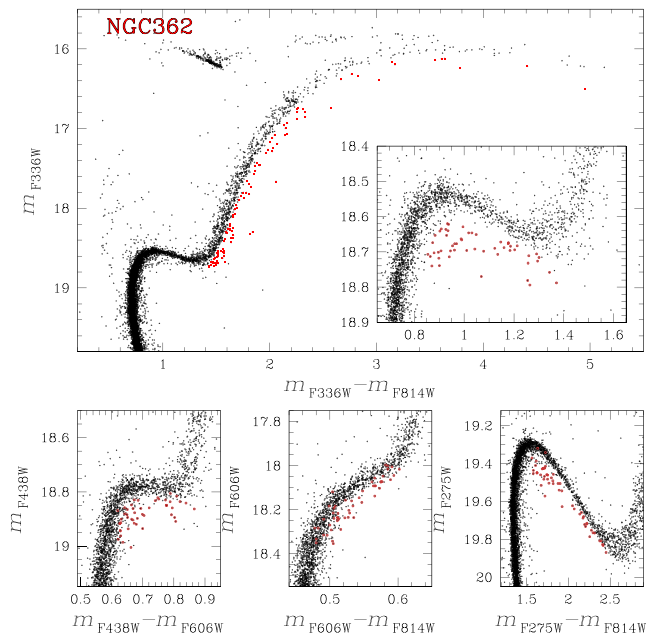


Figure 15. As in Fig. 10 but for NGC 362.

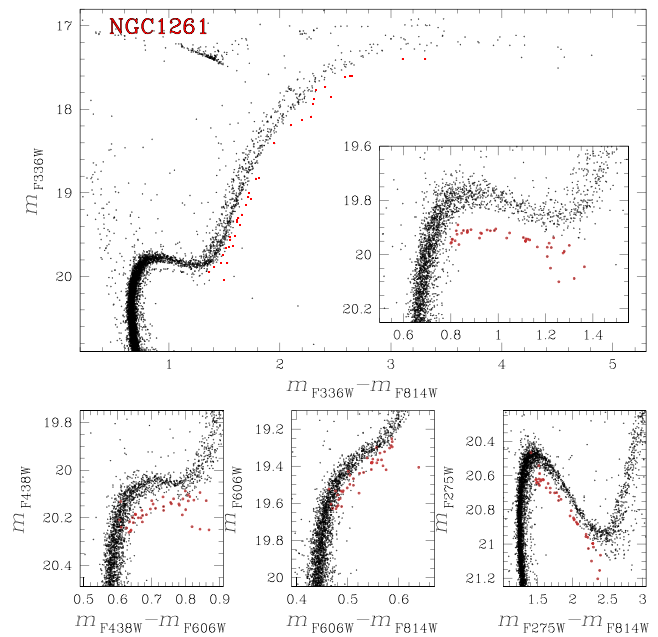


Figure 17. As in Fig. 10 but for NGC 1261.

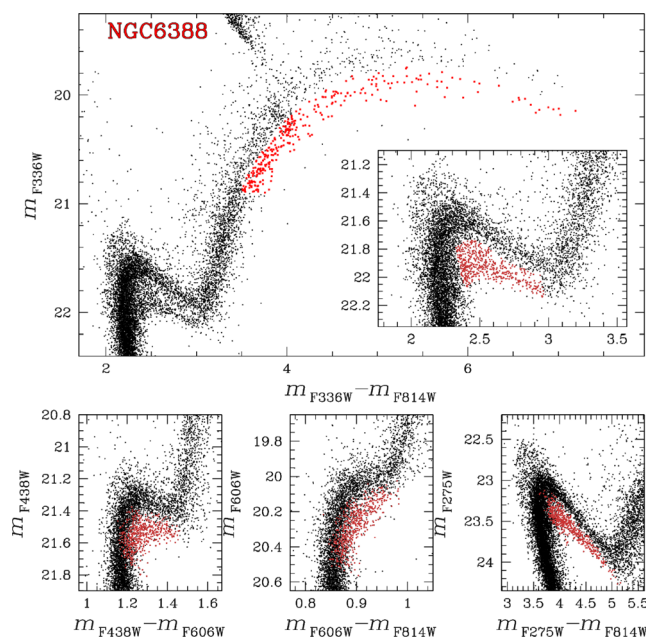


Figure 16. As in Fig. 10 but for NGC 6388.

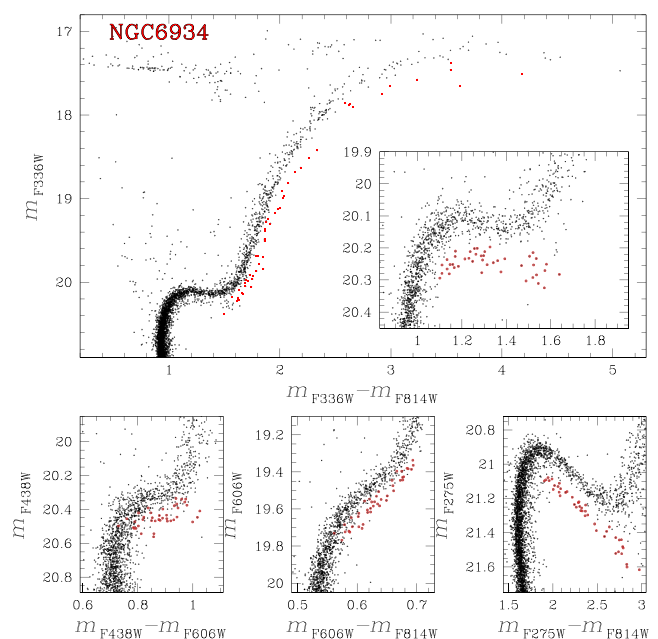


Figure 18. As in Fig. 10 but for NGC 6934.

core ($f_{\text{bin}}^{\text{C}}$), in the region between the core and the half-mass radius ($f_{\text{bin}}^{\text{C-HM}}$), and beyond the half-mass radius ($f_{\text{bin}}^{\text{O-HM}}$).

GC ages have been taken from Marín Franch et al. (2009, hereafter MF09), Dotter et al. (2010, hereafter D10) and Vandenberg et al. (2013, hereafter V13). All ages were obtained by using the same ACS/WFC data set from Sarajedini et al. (2007) and Anderson et al. (2008) that we used in this paper, but different authors employed different sets of isochrones. The Dotter et al. (2010) sample includes 50 of the GCs studied in this paper. Additional ages for six other GCs were derived by Aaron Dotter by using the same method and are published in Milone et al. (2014).

The most recent age compilation comes from Vandenberg et al. (2013) and is based on an improved version of the classical ‘vertical

method’, i.e. the luminosity difference between the zero-age HB and the MS turnoff. These authors have compared Victoria–Regina isochrones with GO-10775 photometry to derive the ages for 51 of the GCs that we have analysed in this paper.

When comparing two variables, we estimate the statistical correlation between the two by using the Spearman’s rank correlation coefficient, r . Moreover, we associate to each value of r an uncertainty that is determined by bootstrapping statistics as in Milone et al. (2014). Briefly, we have generated 1000 equal-size resamples of the original data set by randomly sampling with replacement from the observed data set. For each i -th resample, we have determined r_i and considered the 68.27th percentile of the r_i measurements (σ_r) as indicative of the robustness of r .

Table 3. For each couple of quantities we list the Spearman's rank correlation coefficient, the corresponding uncertainty, and the number of clusters used to calculate the correlation coefficient.

| Parameter | $W_{CF275W, F336W, F438W}$ | $\Delta W_{CF275W, F336W, F438W}$ | $W_C^*_{F275W, F336W, F438W}$ | $\Delta W_C^*_{F275W, F336W, F438W}$ | $W_{F275W, F814W}$ | $\Delta W_{F275W, F814W}$ |
|--------------------------------------|----------------------------|-----------------------------------|-------------------------------|--------------------------------------|-------------------------|---------------------------|
| σ_V | 0.30 ± 0.14, 57 | 0.63 ± 0.08, 57 | 0.20 ± 0.15, 56 | 0.54 ± 0.10, 56 | 0.35 ± 0.14, 57 | 0.46 ± 0.12, 57 |
| c | 0.23 ± 0.14, 57 | 0.38 ± 0.13, 57 | 0.18 ± 0.14, 56 | 0.36 ± 0.13, 56 | 0.17 ± 0.14, 57 | 0.31 ± 0.12, 57 |
| μ_V | -0.44 ± 0.12, 57 | -0.61 ± 0.09, 57 | -0.37 ± 0.12, 56 | -0.56 ± 0.11, 56 | -0.41 ± 0.13, 57 | -0.48 ± 0.10, 57 |
| ϵ | 0.08 ± 0.12, 57 | -0.02 ± 0.14, 57 | -0.07 ± 0.13, 56 | -0.04 ± 0.14, 56 | 0.08 ± 0.14, 57 | 0.15 ± 0.14, 57 |
| ρ_0 | 0.44 ± 0.12, 57 | 0.51 ± 0.12, 57 | 0.37 ± 0.14, 56 | 0.45 ± 0.12, 56 | 0.39 ± 0.13, 57 | 0.41 ± 0.12, 57 |
| $\log \tau_c$ | -0.22 ± 0.15, 57 | -0.14 ± 0.15, 57 | -0.19 ± 0.14, 56 | -0.12 ± 0.15, 56 | -0.07 ± 0.15, 57 | 0.01 ± 0.14, 57 |
| $\log \tau_{hm}$ | -0.18 ± 0.15, 57 | 0.17 ± 0.13, 57 | -0.17 ± 0.15, 56 | 0.19 ± 0.14, 56 | -0.01 ± 0.15, 57 | 0.26 ± 0.13, 57 |
| R_{GC} | -0.38 ± 0.12, 57 | 0.02 ± 0.13, 57 | -0.41 ± 0.12, 56 | 0.01 ± 0.13, 56 | -0.30 ± 0.11, 57 | 0.01 ± 0.13, 57 |
| age (MF09) | -0.31 ± 0.12, 56 | 0.07 ± 0.13, 56 | -0.26 ± 0.12, 55 | 0.11 ± 0.13, 55 | -0.26 ± 0.12, 56 | -0.05 ± 0.14, 56 |
| age (D10) | -0.41 ± 0.11, 56 | 0.06 ± 0.15, 56 | -0.39 ± 0.11, 55 | 0.11 ± 0.14, 55 | -0.29 ± 0.13, 56 | 0.11 ± 0.15, 56 |
| age (V13) | -0.54 ± 0.09, 51 | 0.17 ± 0.14, 51 | -0.53 ± 0.10, 51 | 0.18 ± 0.15, 51 | -0.51 ± 0.10, 51 | 0.01 ± 0.15, 51 |
| [Fe/H] | 0.79 ± 0.05, 57 | -0.07 ± 0.14, 57 | 0.79 ± 0.05, 56 | -0.11 ± 0.14, 56 | 0.65 ± 0.09, 57 | -0.03 ± 0.14, 57 |
| M_V | -0.38 ± 0.12, 57 | -0.70 ± 0.07, 57 | -0.29 ± 0.14, 56 | -0.64 ± 0.09, 56 | -0.50 ± 0.12, 57 | -0.68 ± 0.08, 57 |
| $\log \mathcal{M}/\mathcal{M}_\odot$ | 0.60 ± 0.12, 44 | 0.74 ± 0.08, 44 | 0.51 ± 0.13, 43 | 0.68 ± 0.10, 43 | 0.65 ± 0.12, 44 | 0.69 ± 0.09, 44 |
| f_{bin}^C | 0.18 ± 0.17, 34 | -0.40 ± 0.15, 34 | 0.23 ± 0.17, 34 | -0.32 ± 0.15, 34 | 0.12 ± 0.18, 34 | -0.36 ± 0.14, 34 |
| f_{bin}^{C-HM} | -0.08 ± 0.15, 46 | -0.44 ± 0.12, 46 | -0.06 ± 0.15, 46 | -0.42 ± 0.13, 46 | -0.13 ± 0.16, 46 | -0.42 ± 0.11, 46 |
| f_{bin}^{oHM} | -0.29 ± 0.16, 42 | -0.51 ± 0.13, 42 | -0.22 ± 0.16, 41 | -0.44 ± 0.13, 41 | -0.26 ± 0.15, 42 | -0.37 ± 0.14, 42 |
| $S_{RRLyrae}$ | -0.24 ± 0.12, 57 | 0.02 ± 0.15, 57 | -0.26 ± 0.13, 56 | -0.01 ± 0.15, 56 | -0.23 ± 0.13, 57 | -0.14 ± 0.14, 57 |
| $E(B - V)$ | 0.34 ± 0.12, 57 | -0.11 ± 0.14, 57 | 0.31 ± 0.12, 56 | 0.06 ± 0.14, 56 | 0.41 ± 0.12, 57 | 0.22 ± 0.14, 57 |
| N_I/N_{TOT} | -0.41 ± 0.12, 54 | -0.61 ± 0.09, 54 | -0.32 ± 0.13, 53 | -0.54 ± 0.10, 53 | -0.44 ± 0.12, 54 | -0.56 ± 0.09, 54 |
| Parameter | $W_{F275W, F814W}^*$ | $\Delta W_{F275W, F814W}^*$ | N_I/N_{TOT} | $W_{F275W, F814W}^{1G}$ | $W_{F275W, F814W}^{2G}$ | |
| σ_V | 0.26 ± 0.14, 56 | 0.39 ± 0.13, 56 | -0.63 ± 0.09, 54 | 0.12 ± 0.15, 53 | 0.39 ± 0.13, 53 | |
| c | 0.17 ± 0.14, 56 | 0.32 ± 0.12, 56 | -0.54 ± 0.11, 54 | 0.08 ± 0.17, 53 | 0.18 ± 0.14, 53 | |
| μ_V | -0.38 ± 0.13, 56 | -0.46 ± 0.11, 56 | 0.71 ± 0.07, 54 | -0.19 ± 0.14, 53 | -0.42 ± 0.12, 53 | |
| ϵ | 0.07 ± 0.13, 56 | 0.13 ± 0.13, 56 | -0.07 ± 0.14, 54 | 0.15 ± 0.14, 53 | 0.24 ± 0.13, 53 | |
| ρ_0 | 0.37 ± 0.14, 56 | 0.39 ± 0.12, 56 | -0.63 ± 0.09, 54 | 0.11 ± 0.15, 53 | 0.37 ± 0.13, 53 | |
| $\log \tau_c$ | -0.08 ± 0.15, 56 | -0.01 ± 0.14, 56 | 0.26 ± 0.15, 54 | 0.04 ± 0.16, 53 | 0.03 ± 0.15, 53 | |
| $\log \tau_{hm}$ | -0.03 ± 0.15, 56 | 0.26 ± 0.13, 56 | -0.14 ± 0.15, 54 | 0.20 ± 0.16, 53 | 0.17 ± 0.16, 53 | |
| R_{GC} | -0.29 ± 0.14, 56 | 0.02 ± 0.14, 56 | -0.05 ± 0.13, 54 | 0.02 ± 0.16, 53 | -0.24 ± 0.13, 55 | |
| age (MF09) | -0.25 ± 0.13, 55 | -0.01 ± 0.14, 55 | 0.11 ± 0.15, 53 | -0.36 ± 0.11, 52 | -0.08 ± 0.12, 52 | |
| age (D10) | -0.30 ± 0.12, 55 | 0.16 ± 0.15, 55 | 0.08 ± 0.13, 53 | -0.24 ± 0.13, 52 | -0.10 ± 0.13, 52 | |
| age (V13) | -0.53 ± 0.10, 51 | 0.02 ± 0.16, 51 | 0.06 ± 0.14, 49 | -0.49 ± 0.11, 49 | -0.23 ± 0.14, 49 | |
| [Fe/H] | 0.67 ± 0.08, 56 | -0.08 ± 0.15, 56 | -0.08 ± 0.15, 54 | 0.45 ± 0.13, 53 | 0.47 ± 0.12, 53 | |
| M_V | -0.43 ± 0.12, 56 | -0.63 ± 0.09, 56 | 0.72 ± 0.07, 54 | -0.38 ± 0.13, 53 | -0.59 ± 0.10, 53 | |
| $\log \mathcal{M}/\mathcal{M}_\odot$ | 0.58 ± 0.14, 43 | 0.64 ± 0.09, 43 | -0.81 ± 0.05, 43 | 0.41 ± 0.13, 42 | 0.72 ± 0.09, 42 | |
| f_{bin}^C | 0.17 ± 0.17, 34 | -0.36 ± 0.14, 34 | 0.50 ± 0.17, 33 | -0.02 ± 0.20, 33 | -0.08 ± 0.19, 33 | |
| f_{bin}^{C-HM} | -0.11 ± 0.16, 46 | -0.43 ± 0.10, 46 | 0.58 ± 0.11, 45 | -0.08 ± 0.17, 45 | -0.32 ± 0.15, 45 | |
| f_{bin}^{oHM} | -0.19 ± 0.16, 41 | -0.30 ± 0.14, 41 | 0.65 ± 0.12, 40 | 0.27 ± 0.16, 39 | -0.32 ± 0.15, 39 | |
| $S_{RRLyrae}$ | -0.25 ± 0.13, 56 | -0.15 ± 0.14, 56 | -0.08 ± 0.14, 54 | 0.17 ± 0.14, 55 | -0.13 ± 0.13, 53 | |
| $E(B - V)$ | 0.37 ± 0.13, 56 | 0.19 ± 0.16, 55 | 0.11 ± 0.14, 54 | 0.07 ± 0.15, 53 | 0.29 ± 0.29, 53 | |
| N_I/N_{TOT} | -0.36 ± 0.13, 53 | -0.49 ± 0.11, 52 | 1.00, 54 | -0.25 ± 0.14, 53 | -0.59 ± 0.10, 53 | |

6.1 RGB width and global cluster parameters

Table 3 lists the Spearman's rank correlation coefficients of the $W_{CF275W, F336W, F438W}$ RGB width with all the GC global parameters just listed above. The table also provides the number of clusters used for each determination of r , given in each column after the error on r . There is no significant correlation between the intrinsic RGB width and most of the global parameters, but a strong correlation ($r = 0.79 \pm 0.05$) exists between $W_{CF275W, F336W, F438W}$ and metallicity, as shown in the left-hand panel of Fig. 20. This is hardly

surprising, as at low metallicity the RGB colours become almost insensitive to metal abundances while the RGB-colour sensitivity to composition increases with increasing metallicity.

There is only a mild correlation between the RGB width and the cluster absolute luminosity ($r = -0.38 \pm 0.12$), when using the entire sample of GCs, as shown in the right-hand panel of Fig. 20. However, we note that GCs with almost the same [Fe/H] exhibit quite different $W_{CF275W, F336W, F438W}$ values, thus suggesting that at least one more parameter is controlling the RGB width. Indeed, in the left-hand panel of Fig. 20 we have marked with red dots GCs

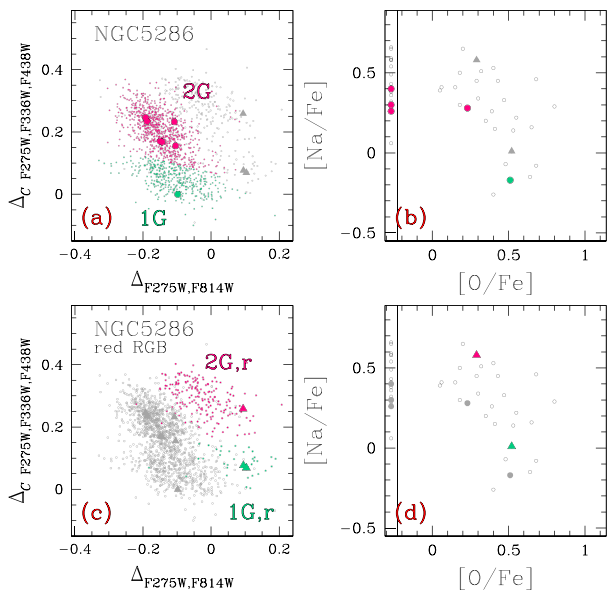


Figure 19. In the chromosome map of NGC 5286, shown in panel (a) only stars from the blue-RGB are used, i.e. those coloured black in Fig. 12. Aqua and magenta colours highlight 1G and 2G stars, respectively, with stars also studied spectroscopically are represented by large filled symbols and whose [Na/Fe] versus [O/Fe] plot from Marino et al. (2015) is shown in panel (b). Finally, in panel (c) the red-RGB stars are coloured either aqua or red for being considered the first or the second generation (1G,r and 2G,r) of the iron-rich population, while panel (d) shows the corresponding [Na/Fe] versus [O/Fe] from Marino et al. (2015).

fainter than $M_V > -7.3$. Clearly the RGB width also depends on the cluster luminosity (or mass).

Low-mass clusters clearly exhibit, on average, smaller $W_{CF275W, F336W, F438W}$ values than more luminous, more massive GCs and define a tighter $W_{CF275W, F336W, F438W}$ versus [Fe/H] correlation ($r = 0.85 \pm 0.07$). The significance of the correlation between RGB width and M_V becomes evident when distinguishing different metallicity ranges, as done in the right-hand panel of Fig. 20. We found $r = 0.76 \pm 0.13$ and $r = 0.82 \pm 0.11$ for the selected groups of metal-rich and metal-poor GCs, respectively, and $r = 0.73 \pm 0.10$ for GCs with $-2.0 < [\text{Fe}/\text{H}] \leq -1.5$. The correlation coefficient has lower values for metal-intermediate GCs with $-1.5 < [\text{Fe}/\text{H}] \leq -1.0$ and corresponds to $r = 0.45 \pm 0.22$.

To further investigate the correlation between the width $W_{CF275W, F336W, F438W}$ and global cluster parameters, we need to remove the dependence on metallicity. Thus, we have least-squares fitted the $W_{CF275W, F336W, F438W}$ versus [Fe/H] relation for GCs with $M_V > -7.3$ with a straight line, as shown in the left-hand panel of Fig. 20, where the best-fitting line is given by $W_{CF275W, F336W, F438W} = 0.14 \pm 0.02 [\text{Fe}/\text{H}] + 0.44 \pm 0.03$. We have then calculated the residuals $\Delta W_{CF275W, F336W, F438W}$ with respect to this line. The values of the resulting Spearman’s rank correlation coefficient are listed in Table 3 for each relation involving $\Delta W_{CF275W, F336W, F438W}$. As expected, $\Delta W_{CF275W, F336W, F438W}$ strongly correlates with the absolute luminosity and with the cluster mass (lower panels of Fig. 20 ($r > 0.7$)).

The $W_{F275W, F814W}$ RGB width has then been analysed in close analogy with what done for $W_{CF275W, F336W, F438W}$. As reported in Table 3, there is a positive correlation between $W_{CF275W, F814W}$ and the cluster metallicity ($r = 0.65 \pm 0.08$), see also the left-hand panel of Fig. 21, where the less massive clusters with $M_V > -7.3$ are marked with red dots. The least-squares best-fitting straight line

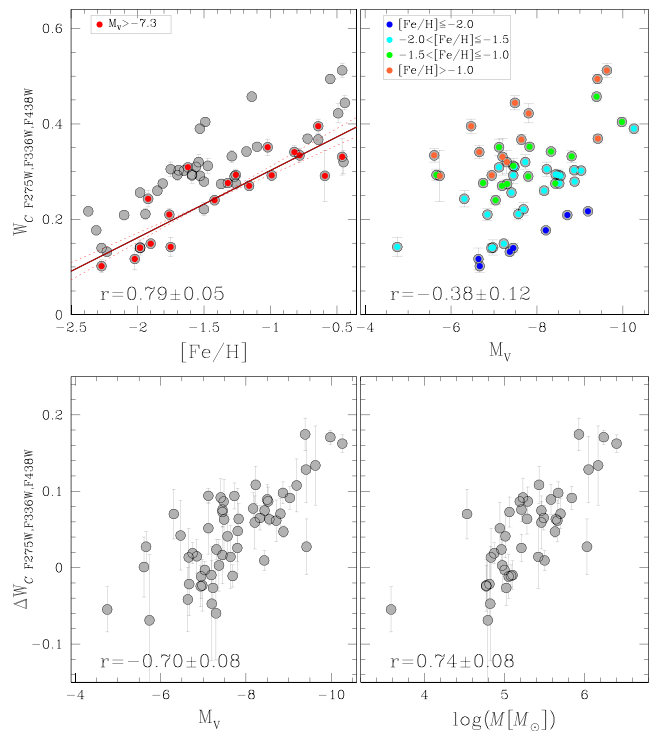


Figure 20. Upper-left panel: the intrinsic RGB width, $W_{CF275W, F336W, F438W}$, as a function of the iron abundance of the host GCs. The red line is the least-squares best-fitting for the faint, less massive clusters with absolute magnitude $M_V > -7.3$, that are marked with red dots. Upper-right panel: the $W_{CF275W, F336W, F438W}$ RGB width versus the absolute visual magnitude M_V of the host clusters. Clusters are colour-coded depending on their metallicity [Fe/H] as indicated in the insert. Lower panels: the residuals of the RGB width, $\Delta W_{CF275W, F336W, F438W}$, against the absolute magnitude (left) and the mass (right) of the host clusters. The Spearman’s rank correlation coefficient (r) and the corresponding uncertainty are reported in each panel.

for the group of GCs with $M_V > -7.3$ is plotted in red in the left-hand panel of Fig. 21 and the residuals $\Delta W_{F275W, F814W}$ with respect to such line are plotted as a function of cluster luminosity and mass in the two panels on the right of the same figure. Strong correlations of such residuals with cluster luminosity and mass are quite evident. We have investigated the relation between $\Delta W_{F275W, F814W}$ and the other global cluster parameters, but no other significant correlation appears to exist, as reported in Table 3.

6.2 Fraction of 1G stars and global cluster parameters

In this section, we investigate univariate relations between the population ratio N_1/N_{TOT} and the global parameters of the host GCs, in analogy with what has been done for the RGB width. The results are reported in Table 3.

The most relevant result is plotted in Fig. 22, which shows significant anticorrelations between the N_1/N_{TOT} ratio and the absolute luminosity and mass of the host clusters (with $r = -0.72 \pm 0.07$ and $r = -0.81 \pm 0.05$, respectively), with more massive GCs having, on average, a smaller fraction of 1G stars. Based on a more limited data set, it had been previously claimed that there is no correlation between the population ratio and cluster mass (Bastian & Lardo 2015). On the contrary, the N_1/N_{TOT} ratio correlates or anticorrelates with several quantities that are closely related with the cluster luminosity and mass. The values of the Spearman’s rank correlation

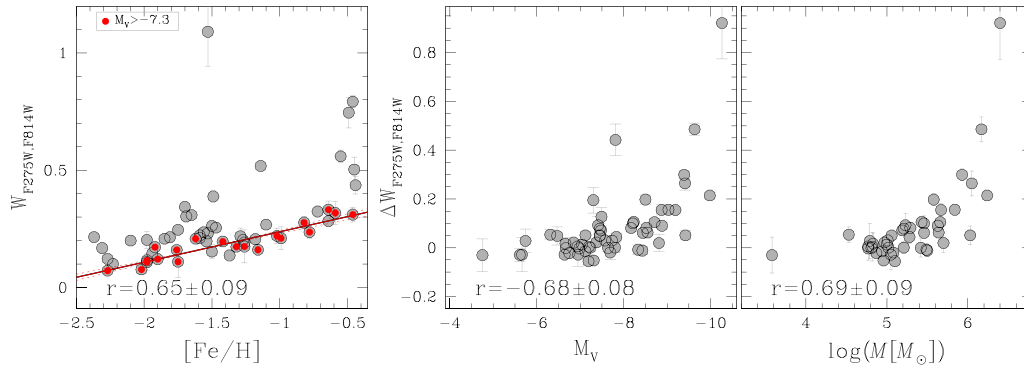


Figure 21. The left-hand panel shows the intrinsic RGB width, $W_{F275W, F814W}$, as a function of metallicity of the host GC. The red line is the best-fitting straight line for clusters with $M_V > -7.3$ that we have represented with red dots. The residuals of the RGB width with respect to the best-fitting line, $\Delta W_{F275W, F814W}$, are plotted against the absolute visual magnitude and the cluster mass in the middle and the right-hand panels, respectively. The Spearman’s rank correlation coefficient and the corresponding uncertainty are reported in each panel. The outlier point refers to ω Centauri.

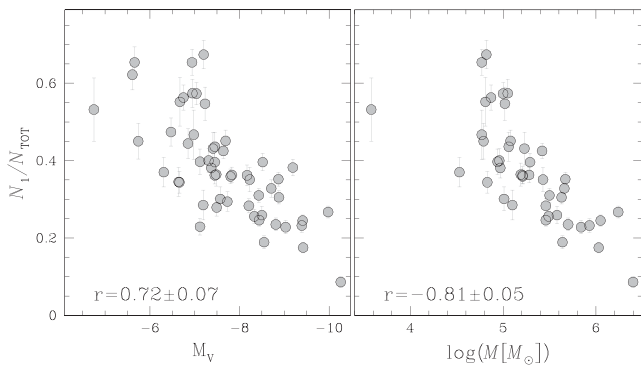


Figure 22. The fraction of 1G stars with respect of the total number of used RGB stars as a function of the cluster absolute luminosity (left), cluster mass (right).

coefficient listed in Table 3 indicate a significant correlation with the central surface brightness (μ_V , in mag arcsec $^{-2}$, $r = 0.71 \pm 0.07$) and significant anticorrelations with the central stellar density ρ_0 ($r = -0.63 \pm 0.09$) and the central velocity dispersion σ_V ($r = -0.63 \pm 0.09$).

We find no significant correlations between the fraction of 1G stars and other global parameters, in particular between the population ratio and the distance from the Galactic centre ($r = -0.05 \pm 0.13$) or with the cluster metallicity ($r = -0.08 \pm 0.15$).

6.3 The $\Delta_{F275W, F814W}$ colour extension of 1G and 2G stars and global cluster parameters

We did not find any strong correlation between $W_{F275W, F814W}^{1G}$ and any of the parameters that we have investigated. There is some mild correlation ($r \sim 0.5$) with the GC metallicity, the cluster mass, and with GC ages ($r = -0.49 \pm 0.11$), but only when ages from Vandenberg et al. (2013) are used. In summary, it is still unclear what controls the $\Delta_{F275W, F814W}$ extension of 1G stars.

In contrast, as shown in Fig. 23, $W_{F275W, F814W}^{2G}$ correlates with cluster mass and luminosity. Moreover, there is some anticorrelation with the fraction of 1G stars ($r = 0.59 \pm 0.10$), which indicates that clusters with a predominant 2G also have wide RGB width in the $F275W-F814W$ colour. There is no strong correlation between $W_{F275W, F814W}^{2G}$ and the cluster metallicity ($r = 0.35 \pm 0.11$), although

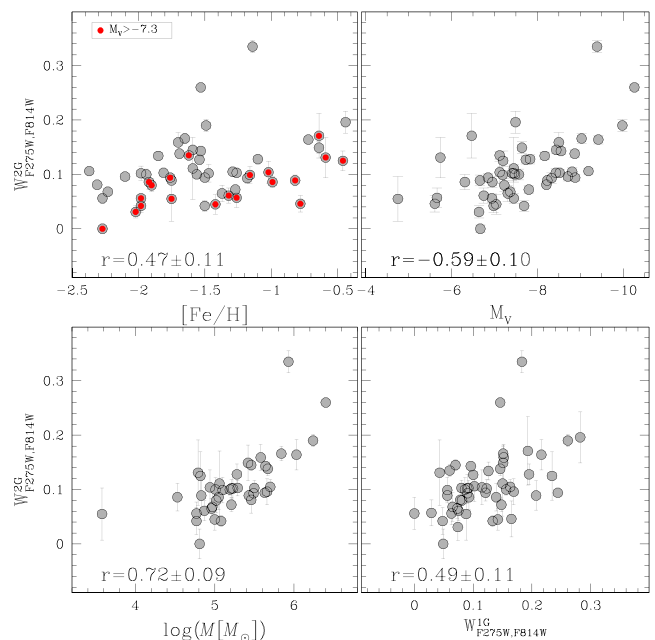


Figure 23. The intrinsic width $W_{F275W, F814W}^{2G}$ of the 2G stars as a function of cluster metallicity and absolute magnitude (upper-left and -right panels, respectively), and as a function of the cluster mass and of the intrinsic width of 1G stars (lower-left and -right panels, respectively). Symbols are like in Fig. 20. The Spearman’s rank correlation coefficient and the corresponding uncertainty are indicated in each panel.

metal-rich GCs with $M_V > -7.3$ have on average larger values of $W_{F275W, F814W}^{2G}$ than metal-poor clusters within the same luminosity range. Similarly, there is only a mild correlation between the extension of the two generations, $W_{F275W, F814W}^{2G}$ and $W_{F275W, F814W}^{1G}$ ($r = 0.49 \pm 0.11$).

7 SUMMARY AND CONCLUSIONS

We have analysed high-precision multiband *HST* photometry of 57 GCs in order to identify and characterize their multiple stellar populations along the RGB. The photometry has been collected through the $F275W$, $F336W$, $F438W$ filters of WFC3/UVIS and the

$F606W$ and $F814W$ filters of WFC/ACS mostly as part of the *HST* UV Legacy Survey of Galactic GCs (Paper I). Archive data have also been used. The main results can be summarized as follows.

(i) From the m_{F814W} versus $C_{F275W, F336W, F438W}$ pseudo-CMD and the m_{F814W} versus $m_{F275W} - m_{F814W}$ CMD of each cluster, which are both very sensitive to multiple stellar populations, we have calculated the RGB width in $C_{F275W, F336W, F438W}$ ($W_{C_{F275W, F336W, F438W}}$) and in $m_{F275W} - m_{F814W}$ ($W_{m_{F275W, F814W}}$). In all 57 GCs, the observed RGB width is significantly wider than expected from observational errors alone. This demonstrates that none of the studied GCs is consistent with hosting a simple stellar population. Among them, ω Centauri, ($M = 10^{6.40} M_{\odot}$) and NGC 6535 ($M = 10^{3.58} M_{\odot}$) are, respectively, the most massive and the least-massive GC of the sample where multiple stellar populations have been detected to date.

(ii) For each cluster we have combined the $C_{F275W, F336W, F438W}$ pseudo-colour and of the $m_{F275W} - m_{F814W}$ colour to construct the $\Delta_{C_{F275W, F336W, F438W}}$ versus $\Delta_{m_{F275W, F814W}}$ pseudo-two-colour diagram, or ‘chromosome map’, which maximizes the information on multiple stellar populations.

(iii) The chromosome maps of the majority of the GCs shows two major, well-separated groups of stars that we identify with first and second generation (1G and 2G). 1G stars are distributed around the origin of the chromosome map and span a narrow range of $\Delta_{C_{F275W, F336W, F438W}}$ values. The group of 2G stars that includes the remaining RGB stars span a wide range of both $\Delta_{C_{F275W, F336W, F438W}}$ and $\Delta_{m_{F275W, F814W}}$ values. Such a clean 1G/2G separation is not possible for a few GCs (namely, NGC 5927, NGC 6304, and NGC 6441), where the two sequences appear to be inextricably merged into a single sequence. Collectively, these clusters (with or without a clear 1G/2G separation) are called type-I clusters.

(iv) The chromosome maps of a second group of clusters, called type-II clusters, show a more complex pattern, with an apparent split of both 1G and 2G sequences. A careful examination of multiband CMDs of all these clusters reveals that their SGBs are split also in purely optical CMDs, while the SGB of type-I GCs splits only in CMDs based on ultraviolet filters. By using spectroscopic data from the literature, we showed that type-II clusters host populations that are also enriched in overall CNO abundance (C+N+O) and heavy elements, such as iron and s-process elements. In particular, it is shown that the faint SGB corresponds to the stellar population enhanced in heavy elements (e.g. Marino et al. 2011). We argue that (1) split 1G and 2G sequences in the chromosome maps, (2) split SGBs, and (3) non-uniformity of the iron and s-elements abundances must be physically connected to each other. This evidence indicates that chromosome maps are an efficient tool to identify GCs with internal variations of heavy elements. In this way, we have identified two new type-II GCs, namely NGC 1261 and NGC 6934.

(v) We use spectroscopic evidence from the literature to show that the photometrically selected 1G and 2G stars are oxygen-rich and sodium-poor and oxygen-poor and sodium-rich, respectively, supporting our identification of 1G and 2G stars with the first and second stellar generation, respectively. However, the number of stars with both accurate *HST* multiband photometry and spectroscopic chemical analysis is still quite scanty. An extensive chemical tagging of multiple populations identified on the chromosome maps is now becoming a major requirement to further progress in the field of stellar populations in GCs.

(vi) Noticeably, the colour width of both 1G and 2G stars in most GCs is significantly wider than what observational errors would suggest. Such evidence demonstrates that in most GCs even

the first (1G) stellar generation is not consistent with a simple, chemically homogeneous stellar population. Again, spectroscopic chemical tagging of 1G stars is needed to identify the origin of their wide range of $\Delta_{F275W, F814W}$ values.

(vii) We have investigated univariate relations between the RGB width in the $W_{F275W, F814W}$ colour and in the $W_{C_{F275W, F336W, F438W}}$ pseudo-colour and the main global parameters of the host GCs. The RGB width mostly correlates with cluster metallicity. After removing the dependence on metallicity, significant correlations emerge between the RGB width and cluster mass and luminosity. These results indicate that massive GCs exhibit more pronounced internal variations of helium and light elements compared with low-mass GCs.

(viii) For each cluster the $F275W-F814W$ colour width of 1G and 2G stars ($W_{F275W, F814W}^{1G(2G)}$) have been measured. No significant correlation has been recovered between $W_{F275W, F814W}^{1G}$ and any of the global cluster parameters. In contrast $W_{F275W, F814W}^{2G}$ correlates with the cluster mass.

(ix) We have measured the fraction of 1G RGB stars with respect to the total number of RGB stars. The N_{1G}/N_{TOT} ratio ranges from ~ 0.08 in the case of ω Centauri to ~ 0.67 . There is a significant anticorrelation between the fraction of 1G stars and the mass of the host cluster, with massive GCs hosting a smaller fraction of 1G stars. Hence, the multiple population phenomenon appears to systematically increase in incidence and complexity with increasing cluster mass.

(x) In some cases distinct stellar clumps are clearly present along the sequence of 1G and/or 2G stars, while in other clusters we observe a smooth distribution without evident clumps. However, a large number of stars is needed to unambiguously identify distinct subpopulations along the MSs in the chromosome maps, as done in Paper II and Paper III for NGC 7089 and NGC 2808, respectively.

ACKNOWLEDGEMENTS

Support for *Hubble Space Telescope* proposal GO-13297 was provided by NASA through grants from Space Telescope Science Institute (STScI), which is operated by Association of Universities for Research in Astronomy (AURA), Inc., under National Aeronautics and Space Administration (NASA) contract NAS 5-26555. We thank the anonymous referee for her/his suggestions that have improved the quality of the paper. APM and AFM acknowledge support by the Australian Research Council through Discovery Early Career Researcher Awards DE150101816 and DE160100851. GP, AR, FD, and SC acknowledge financial support by PRIN-INAF2014 (PI: Cassisi).

REFERENCES

- Anderson J., Bedin L. R., 2010, *PASP*, 122, 1035
 Anderson J., King I. R., 2003, *AJ*, 126, 772
 Anderson J., King I. R., 2006, Instrument Science Report ACS 2006-01, 1
 Anderson J. et al., 2008, *AJ*, 135, 2055
 Bastian N., Lardo C., 2015, *MNRAS*, 453, 357
 Bedin L. R., Piotto G., Anderson J., Cassisi S., King I. R., Momany Y., Carraro G., 2004, *ApJ*, 605, L125
 Bedin L. R., Cassisi S., Castelli F., Piotto G., Anderson J., Salaris M., Momany Y., Pietrinferni A., 2005, *MNRAS*, 357, 1038
 Bellini A., Piotto G., Bedin L. R., King I. R., Anderson J., Milone A. P., Momany Y., 2009, *A&A*, 507, 1393

Bellini A., Anderson J., Bedin L. R., 2011, *PASP*, 123, 622
 Bellini A. et al., 2013, *ApJ*, 765, 32
 Bellini A. et al., 2015, *ApJ*, 810, L13
 Brown T. M. et al., 2016, *ApJ*, 822, 44
 Carretta E., Bragaglia A., Gratton R. G., Leone F., Recio-Blanco A., Lucatello S., 2006, *A&A*, 450, 523
 Carretta E. et al., 2009, *A&A*, 505, 117
 Carretta E., Gratton R. G., Bragaglia A., D’Orazi V., Lucatello S., 2013, *A&A*, 550, A34
 Cassisi S., Salaris M., Pietrinferni A., Piotto G., Milone A. P., Bedin L. R., Anderson J., 2008, *ApJ*, 672, L115
 Cordero M. J., Pilachowski C. A., Johnson C. I., McDonald I., Zijlstra A. A., Simmerer J., 2014, *ApJ*, 780, 94
 D’Antona F., Vesperini E., D’Ercole A., Ventura P., Milone A. P., Marino A. F., Tailo M., 2016, *MNRAS*, 458, 2122
 Decressin T., Meynet G., Charbonnel C., Prantzos N., Ekström S., 2007, *A&A*, 464, 1029
 Dotter A. et al., 2010, *ApJ*, 708, 698 (D10)
 Gilliland R. L., 2004, Instrument Science Report ACS 2004-01, 17
 Han S.-I., Lee Y.-W., Joo S.-J., Sohn S. T., Yoon S.-J., Kim H.-S., Lee J.-W., 2009, *ApJ*, 707, L190
 Harris W. E., 1996, *AJ*, 112, 1487
 Ivans I. I., Sneden C., Kraft R. P., Suntzeff N. B., Smith V. V., Langer G. E., Fulbright J. P., 1999, *AJ*, 118, 1273
 Johnson C. I., Pilachowski C. A., 2010, *ApJ*, 722, 1373
 Johnson C. I., Rich R. M., Pilachowski C. A., Caldwell N., Mateo M., Bailey J. I., III, Crane J. D., 2015, *AJ*, 150, 63
 McLachlan G., Peel D., 2000, *Finite Mixture Models*, Wiley, New York
 McLaughlin D. E., van der Marel R. P., 2005, *ApJS*, 161, 304
 Marín Franch A. et al., 2009, *ApJ*, 694, 1498 (MF09)
 Marino A. F., Villanova S., Piotto G., Milone A. P., Momany Y., Bedin L. R., Medling A. M., 2008, *A&A*, 490, 625
 Marino A. F., Milone A. P., Piotto G., Villanova S., Bedin L. R., Bellini A., Renzini A., 2009, *A&A*, 505, 1099
 Marino A. F. et al., 2011, *A&A*, 532, A8
 Marino A. F. et al., 2012, *ApJ*, 746, 14
 Marino A. F. et al., 2015, *MNRAS*, 450, 815
 Milone A. P., 2015, *MNRAS*, 446, 1672
 Milone A. P. et al., 2008, *ApJ*, 673, 241
 Milone A. P., Piotto G., Bedin L. R., Cassisi S., Anderson J., Marino A. F., Pietrinferni A., Aparicio A., 2012a, *A&A*, 537, A77
 Milone A. P. et al., 2012b, *ApJ*, 744, 58
 Milone A. P. et al., 2013, *ApJ*, 767, 120
 Milone A. P. et al., 2014, *ApJ*, 785, 21
 Milone A. P. et al., 2015a, *MNRAS*, 447, 927 (Paper II)
 Milone A. P. et al., 2015b, *ApJ*, 808, 51 (Paper III)
 Nardiello D. et al., 2015, *MNRAS*, 451, 312
 Piotto G. et al., 2012, *ApJ*, 760, 39
 Piotto G., Milone A. P., Marino A. F., Bedin L. R., Anderson J., Jerjen H., Bellini A., Cassisi S., 2013, *ApJ*, 775, 15
 Piotto G. et al., 2015, *AJ*, 149, 91 (Paper I)
 Renzini A. et al., 2015, *MNRAS*, 454, 4197
 Rich R. M. et al., 1997, *ApJ*, 484, L25
 Sarajedini A. et al., 2007, *AJ*, 133, 1658
 Silverman B. W., 1986, *Monographs on Statistics and Applied Probability*. Chapman and Hall, London
 Sollima A., Ferraro F. R., Bellazzini M., Origlia L., Straniero O., Pancino E., 2007, *ApJ*, 654, 915
 Trager S. C., King I. R., Djorgovski S., 1995, *AJ*, 109, 218
 Vandenberg D. A., Brogaard K., Leaman R., Casagrande L., 2013, *ApJ*, 775, 134 (V13)
 Ventura P., Caloi V., D’Antona F., Ferguson J., Milone A., Piotto G. P., 2009, *MNRAS*, 399, 934
 Villanova S., Geisler D., Gratton R. G., Cassisi S., 2014, *ApJ*, 791, 107
 Wilson C. P., 1975, *AJ*, 80, 175
 Yong D., Grundahl F., D’Antona F., Karakas A. I., Lattanzio J. C., Norris J. E., 2009, *ApJ*, 695, L62

Yong D. et al., 2014, *MNRAS*, 441, 3396

Yong D., Da Costa G. S., Norris J. E., 2016, *MNRAS*, 460, 1846

APPENDIX A: THE CONSTRUCTION OF THE CHROMOSOME MAP OF ω CENTAURI

ω Centauri shows the most complex chromosome map. The distribution of the stars that we have coloured black in Fig. 6 resembles that of some GCs with single SGB like NGC 6723 or NGC 2808. In contrast, red-RGB stars exhibit an unique pattern, with three main streams of red-RGB stars. The most populous RGB starts from $(\Delta_{F275W, F814W}; \Delta_{F275W, F336W, F438W}) \sim (-0.2; 0.35)$ and extends towards extreme values of $\Delta_{F275W, F814W} \sim 1.5$. A second stream ranges from $(\Delta_{F275W, F814W}; \Delta_{F275W, F336W, F438W}) \sim (0.0; 0.1)$ to $(1.5; -0.4)$ and possibly includes a few stars with even larger $\Delta_{F275W, F814W}$. A third stream has intermediate $\Delta_{F275W, F814W}$ and $\Delta_{F275W, F336W, F438W}$ values with respect to the previous two.

Each stream includes substellar populations. In an attempt to estimate how many groups of stars are statistically significant in ω Centauri, we used the `MCLUSTER CRAN` package in the public domain R statistical software system. This package performs a maximum likelihood fits to different number of stellar groups by using several different assumptions about shape and size of the different populations in the chromosome map, and evaluate the number of groups by the Bayesian Information Criterion (BIC) penalized likelihood measure for model complexity (see McLachlan & Peel 2000, for details). For each shape and size that we adopted for the populations, we assumed a number, N , of stellar populations from 1 to 20 and estimated a BIC for each combination. The best BIC value corresponds to $N = 16$.

When compared with the other GCs investigated in this paper, ω Centauri exhibits by far the most complex CMD and its RGB spans a very wide range of $m_{F275W} - m_{F814W}$ colour as shown in panel (a1) of Fig. A1. Due to the complex structure of its RGB, in order to derive the chromosome map of ω Centauri, we have adopted an iterative procedure that is based on the method of Section 3.2, and which is illustrated in Fig. A1.

As a first step, we have derived a raw chromosome map by using the same procedure described in Section 3.2. Then, we have identified three groups of stars that have been used to derive the fiducial lines shown in m_{F814W} versus $m_{F275W} - m_{F814W}$ CMD and the m_{F814W} versus $C_{F275W, F336W, F438W}$ pseudo-CMD plotted in panels (a1) and (b1) of Fig. A1. The selected groups of stars are shown in panels (c) and (d) of Fig. A1 where black and orange dots and aqua-starred symbols overlaid on the final chromosome map of ω Centauri represent stars of the samples 1, 2, and 3, respectively.

These three groups of stars have been determined iteratively by using the following criteria. The chromosome map of stars in sample 1 resembles those observed in several GCs in which the stars are distributed along a single sequence and define distinct bumps. Sample 2 includes the bump of stars around $(\Delta_{F275W, F814W}; \Delta_{F275W, F336W, F438W}) \sim (-1.10; 0.35)$, while sample 3 includes most of the stars of the reddest and the most metal-rich RGB of ω Centauri that has been often indicated as population 4 (e.g. Bedin et al. 2004). Noticeably, we have excluded from sample 3 the stars in the poorly populated bump with $(\Delta_{F275W, F814W}; \Delta_{F275W, F336W, F438W}) \sim (0.3; 0.0)$.

In order to derive $\Delta_{F275W, F814W}$ for RGB stars in ω Centauri, we have used the following procedure that is illustrated in panels (a1) and (a2) of Fig. A1. We have first divided the RGB stars in three groups. Group I includes all the RGB stars with bluer $m_{F275W} - m_{F814W}$ colours than the red fiducial line at the corresponding

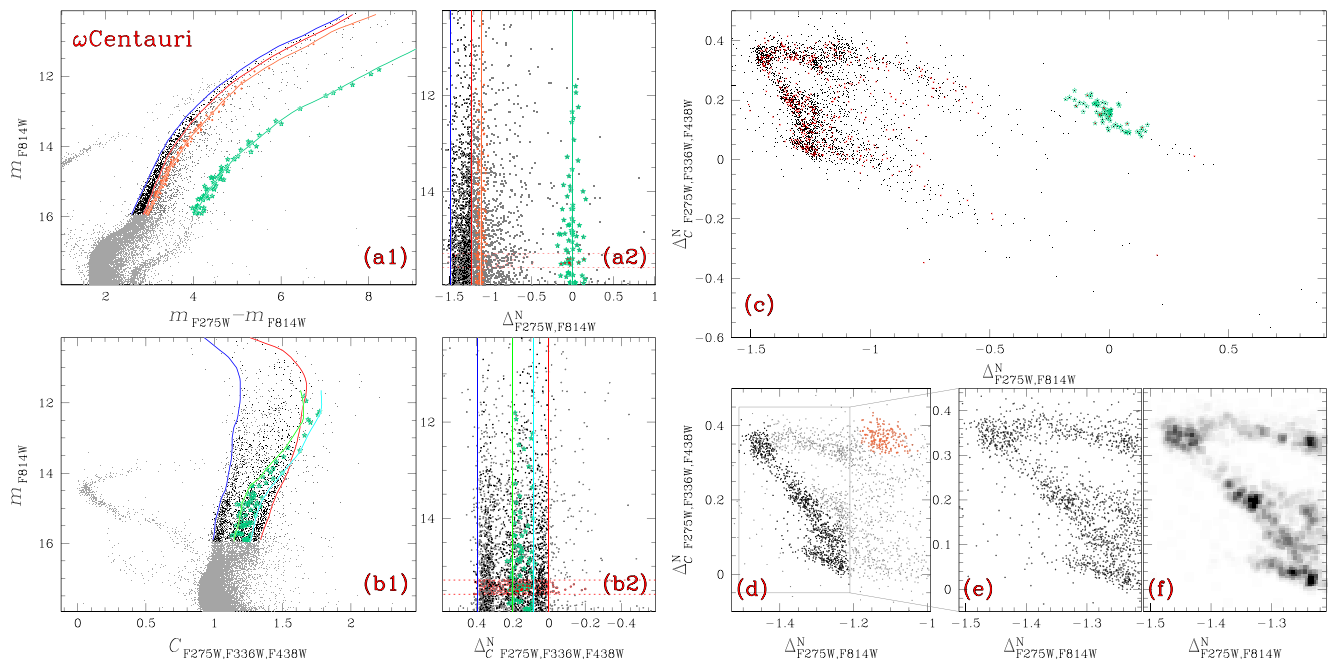


Figure A1. This figure illustrates the procedure used to derive the chromosome map of NGC 5139 (ω Centauri). The m_{F814W} versus $m_{F275W} - m_{F814W}$ CMD and the m_{F814W} versus $C_{F275W, F336W, F438W}$ pseudo-CMD are plotted in panels (a1) and (b1), respectively. Dark-grey and coloured points to mark the sample of analysed RGB stars. The red and the blue lines overimposed on the diagrams of both panels (a1) and (d1) correspond to the red and the blue envelopes of RGB of stars in the sample 1. The orange and the green lines shown in the panel (a1) are the fiducial lines of the samples 2 and 3 of stars. In the panel (b1), we have used green and cyan colours to mark the red and blue edges of the envelope of RGB of sample-3 stars. Panels (a2) and (b2) show the verticalized m_{F814W} versus $\Delta_{CF275W, F336W, F438W}$ and m_{F814W} versus $\Delta_{CF275W, F336W, F438W}$ diagrams for RGB stars. The $\Delta_{CF275W, F336W, F438W}$ versus $\Delta_{NF275W, F814W}$ chromosome map of RGB stars in ω Centauri is shown in panel (c), where red dots represent RGB stars with $15.28 < m_{F814W} < 15.58$ between the two horizontal dotted lines of panels (a2) and (b2). Panels (d) and (e) are zoomed-in view of the chromosome map shown in panel (c), while panel (f) shows the $\Delta_{CF275W, F336W, F438W}$ versus $\Delta_{NF275W, F814W}$ Hess diagram of the stars plotted in panel (e). The aqua-starred symbols plotted in panels (a1), (a2), (b1), (b2), and (c) mark the sample-3 stars, while sample-1 stars are represented with black dots in panels (a1), (a2), (b1), (b2), and (d). The orange dots shown in panels (a1), (a2), and (d) indicate sample-2 stars.

$F814W$ magnitude. Group II includes the RGB stars between the red and the orange line, while the remaining RGB stars belong to group III. The red and the blue fiducial lines shown in panel (a1) are the redder and the bluer envelopes of the RGB formed by sample-1 stars and have been derived as in Section 3.1 by using sample-1 stars only. The orange and the aqua lines shown in panel (a1) are fiducial lines of the RGB made by sample-2 and sample-3 stars. We have derived the quantities $\Delta_{F275W, F814W}^{NI}$, $\Delta_{F275W, F814W}^{NII}$, and $\Delta_{F275W, F814W}^{NIII}$ for stars in the three groups, by using the following equations that are similar to equation (1):

$$\Delta_{F275W, F814W}^{NI(II,III)} = W_{F275W, F814W}^{I(II,III)} \times [(X - X_{\text{fiducialA}}) / (X_{\text{fiducialB}} - X_{\text{fiducialA}})]. \quad (\text{A1})$$

For group-I stars, we have assumed the blue and the red fiducial shown in panel (a1) of Fig. A1 as the fiducial A and fiducial B, respectively. For group-II stars, the red fiducial corresponds to fiducial A and the orange fiducial corresponds to fiducial B, while for group-III stars we used the orange and the green fiducials as fiducial A and B, respectively. The constant $W_{F275W, F814W}^I$ has been derived for group-I stars as in Section 3.1, while $W_{F275W, F814W}^{II}$ has been derived as the $m_{F275W} - m_{F814W}$ colour difference between the orange and the red fiducial line shown in panel (a1) of Fig. A1 calculated 2.0 $F814W$ mag above the MS turnoff. The constant $W_{F275W, F814W}^{III}$ has been derived similarly for group-III star, but by using green and orange fiducials.

We assumed:

$$\begin{aligned} \Delta_{F275W, F814W} &= \Delta_{F275W, F814W}^{NI} \text{ for group-I stars;} \\ \Delta_{F275W, F814W} &= W_{F275W, F814W}^I + \Delta_{F275W, F814W}^{NII} \text{ for group-II stars;} \end{aligned}$$

and

$$\Delta_{F275W, F814W} = W_{F275W, F814W}^I + W_{F275W, F814W}^{II} + \Delta_{F275W, F814W}^{NIII}$$

for group-III stars. The verticalized m_{F814W} versus $\Delta_{F275W, F814W}$ diagram of the analysed RGB stars in ω Centauri is plotted in the panel (a2) of Fig. A1 where the vertical coloured lines corresponds to the fiducial lines shown in panel (a1).

In order to derive $\Delta_{CF275W, F336W, F438W}$ for RGB stars of ω Centauri we adopted the method illustrated in panels (b1) and (b2) of Fig. A1, where the red and blue lines are the boundaries of the RGB for stars in sample 1, while the green and the cyan lines are the boundaries for stars in the sample 3. These lines have been derived as described in Section 3.1.

We proceeded by defining two additional groups of stars. Group IV includes all the RGB stars that are associated with the most metal-rich population of ω Centauri and that have $\Delta_{F275W, F814W} > -0.2$ and $\Delta_{CF275W, F336W, F438W} > -0.1$ in panel (c) of Fig. A1. Group V includes all the remaining RGB stars.

We derived $\Delta_{CF275W, F336W, F438W}^{N,IV}$ for group-IV stars by means of equation (2) and by assuming the green and cyan lines plotted in panel (b1) of Fig. A1 as fiducials A and B, respectively. Similarly, we have calculated $\Delta_{CF275W, F336W, F438W}^{N,V}$ by using equation (2) and assuming that the blue and red lines in the panel (b1) of Fig. A1 correspond to the fiducials A and B, respectively.

We assumed:

$\Delta_{C\ F275W, F336W, F438W} = \Delta_{C\ F275W, F336W, F438W}^{N,IV}$ for group-IV stars and;

$\Delta_{C\ F275W, F336W, F438W} = W_{C\ F275W, F336W, F438W}^{IV-V} + \Delta_{C\ F275W, F336W, F438W}^{N,V}$ for group-V stars, where $W_{C\ F275W, F336W, F438W}^{IV-V}$ is the $C_{F275W, F336W, F438W}$ pseudo-colour difference between the blue and the cyan fiducial line calculated 2.0 $F814W$ magnitudes above the MS turnoff.

The chromosome map has been derived iteratively and four iterations were required to reach convergence. After each iteration, we improved the selection of stars in the samples 1, 2, and 3, derived improved fiducial lines and better estimates of $\Delta_{F275W, F814W}$ and $\Delta_{C\ F275W, F336W, F438W}$.

The chromosome map of ω Centauri is plotted in the panel (c) of Fig. A1 and it reveals a very complex stellar distribution, with the presence of distinct bumps of stars and stellar streams. To verify that the observed structure does not include artefacts introduced by the adopted fiducial lines, we marked in red in panel (c) all the stars

in a small magnitude interval with $15.38 < m_{F814W} < 15.58$ that are placed between the horizontal dotted lines of panels (a2) and (b2). The fact that the selected stars distribute along the entire map demonstrates that the observed stellar bumps and tails are real. Panels (d) and (e) of Fig. A1 are a zoomed-in view of the chromosome map around the region with low values of $\Delta_{F275W, F814W}$, while panel (f) shows the Hess diagram of the same stars plotted in panel (e). These figures reveal that the sample 1 of stars in ω Centauri define a continuous sequence characterized by the presence of distinct stellar bumps, in close analogy with what we observe in NGC 6723. In addition, ω Centauri hosts stellar populations, including bumps and streams, with values of $\Delta_{F275W, F814W}$ larger than those of sample-1 stars with the same $\Delta_{F275W, F336W, F438W}$.

This paper has been typeset from a $\text{\TeX}/\text{\LaTeX}$ file prepared by the author.